VICTORIA UNIVERSITY
MELBOURNE AUSTRALIA

Chlorination of oxybenzone and prediction of transformation products using non-equilibrium "forced" molecular dynamics

This is the Accepted version of the following publication

Chlorination of Oxybenzone and Prediction of Transformation Products Using Non-Equilibrium "Forced" Molecular Dynamics

10 April 2018

Harry Ridgway* | [AquaMem Scientific Consultants](#) | PO Box 251, Rodeo, New Mexico, USA 88056 | Email: ridgway@vtc.net | Ph: +1 575-557-7777 | Mobile: +1 575-654-2813

John Orbell | Institute for Sustainable Industries & Liveable Cities, Victoria University (Werribee campus) | PO Box 14428, Melbourne, Australia, 8001 | Email: john.orbell@vu.edu.au | Ph: +61 3 9919 8066

Stephen Gray | Institute for Sustainable Industries & Liveable Cities, Victoria University | PO Box 14428, Melbourne, Australia, 8001 | Email: Stephen.gray@vu.edu.au | Ph: +61 3 9919 8097 | Mobile: +61 434 605 847

Keywords: benzophenone; chlorine; disinfection; disinfection byproduct; molecular dynamics; molecular modeling; oxybenzone; QM/MM; reaction mechanism; wastewater; water reuse; water treatment

* Corresponding author

Table of Abbreviations:

BPA	bis-phenol_A
DIIS	direct inversion of the iterative subspace
DFT	density functional theory
HOMO	highest occupied molecular orbital
MD	molecular dynamics
MM	molecular mechanics
MO	molecular orbital
NDDO	neglect of diatomic differential overlap; category of semiempircal calculation
NSC	nano-solvation cage
N_{eq}FMD	non-equilibrium forced molecular dynamics
OxBZ	oxybenzone
QM	quantum mechanics
QM/MM	quantum mechanical/molecular mechanics methodology
RM1	semiempirical method similar to AM1 or PM3
S_EAr	electrophilic aromatic substitution reaction mechanism with arenium ion formation
SFC	self-consistent field calculation
STP	standard temperature and pressure
TIP3P	water model of Jorgenson *et al.*, 1983
TP	transformation product
UHF	unrestricted Hartree-Fock

1.0 Abstract:

Oxybenzone (OxBZ) is a member of the benzophenone family of sunscreen filters. Despite its broad biotoxicity, OxBZ and its transformation products (TPs) have been detected in coastal seawater, wastewater and drinking water supplies around the globe. Unfortunately, little is known about the fate of OxBZ during water treatment, especially when exposed to chlorine or ozone disinfection. In this report, a hybrid quantum/molecular mechanics (QM/MM) algorithm is described that simulates reactions between OxBZ and hypochlorous acid (HOCl) in an aqueous background. The algorithm uses non-equilibrium molecular dynamics (N_{eq}FMD) to force bi-molecular collisions between HOCl and OxBZ over a population of random reactant conformations and orientations. A semiempirical QM method (RM1) is used to control and manage reactant collisions and compute molecular orbital (MO) rearrangements leading to bond dissociation and formation, while explicit water is treated Classically as a perturbation on the electronic wave function. The N_{eq}FMD method qualitatively emulated key aspects of aromatic ring activation and substituent directing effects (including an -OCH$_3$ π-σ* hyperconjugation) associated with OxBZ pendent groups. When applied to the solvated HOCl-OxBZ system, a diversity of potential TPs were observed, several of which have been documented in prior experimental studies, including hydroxy radical (•OH), chlorine radical (•Cl), methyl radical (•CH$_3$), formaldehyde (H$_2$C=O; or its *di*-radical precursor •CH$_2$O•), chloromethane (ClCH$_3$), *mono*-chloro-oxybenzone or its *meta*-stable Wheland intermediate, as well as open-ring and ring-scission products such as *mono*-chlorobenzene, *para*-chloromethoxyphenol (chloro-guaiacol) and 4-methoxy-catechol. Halogen addition to the methoxy ring was preceded by homolytic cleavage of HOCl to form an •OH radical + a transitory "semi-bound" •Cl radical. The later underwent nascent covalent bonding to an *ortho*-carbon via π-resonance delocalization to form a *meta*-stable carbocation intermediate expected to devolve by hydrogen abstraction to the monochlorinated *ortho*-substituted OxBZ product observed in experimental studies. Chlorine electron density (which increased over the collision trajectory) delocalized inversely with the mean partial charge of the methoxy ring, as well as the total charge of the OxBZ molecule, consistent with a S$_E$Ar (arenium ion) mechanism. Kinetically-induced conformational strain in OxBZ was accompanied by resonance fluctuations in conjugated π-bonds comprising the methoxy ring, as revealed by coupled interatomic oscillations in sp2 aromatic carbon partial charges. Finally, an unusual *ipso* hydroxylation/*di*-radical mechanism not previously reported is described for the formation of formaldehyde in HOCl-OxBZ collisions. Results indicate that N_{eq}FMD simulations can complement and extend experimental approaches to predict reaction outcomes and assist in the elucidation of reaction mechanisms involved in disinfection byproduct formation.

2.0 Background: Oxybenzone ([2-hydroxy-4-methoxyphenyl-phenylmethanone) is a member of the chemically-related benzophenone family of UV-blocking sunscreen filters [1, 2]. Due to its widespread use globally, oxybenzone (OxBZ) and its transformation products (TPs) have become widely dispersed into the environment; and they have been detected in coastal seawater, municipal wastewater, groundwater and drinking water supplies [3, 4]. Oxybenzone that has entered coastal seawater ecosystems by a variety of pathways including municipal wastewater discharges has been implicated in coral reef toxicity and bleaching [5].

Oxybenzone is an estrogen disrupting compound [6, 7, 8] and phototoxic agent with a number of TPs of health significance formed after exposure to sunlight [2, 3, 9]. Structurally, OxBZ is similar to the plastic additive *bis*-phenol-A (BPA), which is a known human carcinogen [10]. Like BPA, OxBZ and related compounds can form mutagenic and genotoxic metabolic byproducts by photo-oxidative stress responses [9] or DNA-adduct formation involving bio-activation by cytochrome P450 enzymes [11, 12]. Oxybenzone and other benzophenones also increase tumor metastasis potential by inducing proliferation in cancer cell lines via estrogen-mediated [13, 14] and non-estrogenic mechanisms [15].

Little is known about the fate of OxBZ during water treatment, particularly with respect to TP formation following exposure to chlorine disinfection or advanced oxidation processes. Despite several recent studies reporting a range of toxic halogen-addition/substitution and non-halogenated products of OxBZ and other benzophenones in laboratory chlorination experiments, the mechanistic details of TP formation for many of the compounds and intermediates remain sketchy [16-20].

In an effort to better understand the potential fate of OxBZ and its TPs formed during chlorine disinfection in wastewater reuse and potable water treatment processes, we have developed and applied a hybrid quantum/molecular mechanics (QM/MM) non-equilibrium "forced" molecular dynamics (N_{eq}FMD) approach that can be used to rapidly screen for and identify TPs of interest in simulated chlorination reactions. The *in-silico* method was employed to detect potentially stable 1st-generation TPs and transient intermediates formed during the reaction of hypochlorous acid (HOCl) with OxBZ in an aqueous (Newtonian) background. The algorithm robotically executes bi/multi-molecular collisions between reactive species, *e.g.*, an oxidant molecule + a small organic compound, controlled by a semiempirical QM method able to estimate molecular orbital (MO) energies and rearrangements, which in turn emulate bond dissociation and formation events leading to TP formation.

Semiempirical calculations are employed in the N_{eq}FMD method because they are computationally less expensive than *ab initio* or density functional theory (DFT) methods while at the same time providing reasonable accuracy in forecasting all-valence electron MO rearrangements. Suitably parameterized for the molecular species under consideration, semiempirical QM/MM calculations have been successfully applied to solvated inorganic systems [21], as well as enzyme-catalyzed biochemical reactions [22-25]; and they have been

shown to yield results that are frequently comparable to those obtained by *ab initio* and DFT approaches [26-29].

Nevertheless, given the theoretical limitations of semiempirical calculations, which do not explicitly address electron correlation, the N_{eq}FMD algorithm employed in this study *is primarily intended as a first-principles computational screening procedure for predicting potential TP types and their statistical distributions.* An interesting benefit of this approach is that it can be utilized to survey large numbers of potential TPs and identify those of special interest (*e.g.,* biotxic compounds), as well as the precise reactive collision conditions that led to their formation. The N_{eq}FMD simulations may be replayed to elucidate mechanistic details leading to TP formation using the same or additional levels of QM theory. Although the N_{eq}FMD method yields only initial TPs resulting from 1st-generation collisions, it was recently successfully applied to identify several key reaction products and intermediates in gas-phase transformations of sabinene and benzene by ozone [30].

3.0 Methods:

3.1 Modeling Reactant Compounds:
HOCL and OxBZ models were built and optimized using a combination of standard Newtonian mechanics (MM) force fields and self-consistent field (SCF) post Hartree-Fock QM calculation methods provided in Hyperchem Version 8.0.10 (Hypercube, Inc., Gainsville, FL, USA). Following initial 2D sketching, the compounds were converted to approximate 3D structures using Hyperchem's heuristic-based auto-builder and geometry optimized via the Polak-Ribiere conjugate-gradient method by Hyperchem's MM+ Classical force field using bond dipoles to initially describe system electrostatics. Each compound was then re-optimized *in vacuo* using a singlet groundstate SCF Unrestricted Hartree-Fock (UHF)
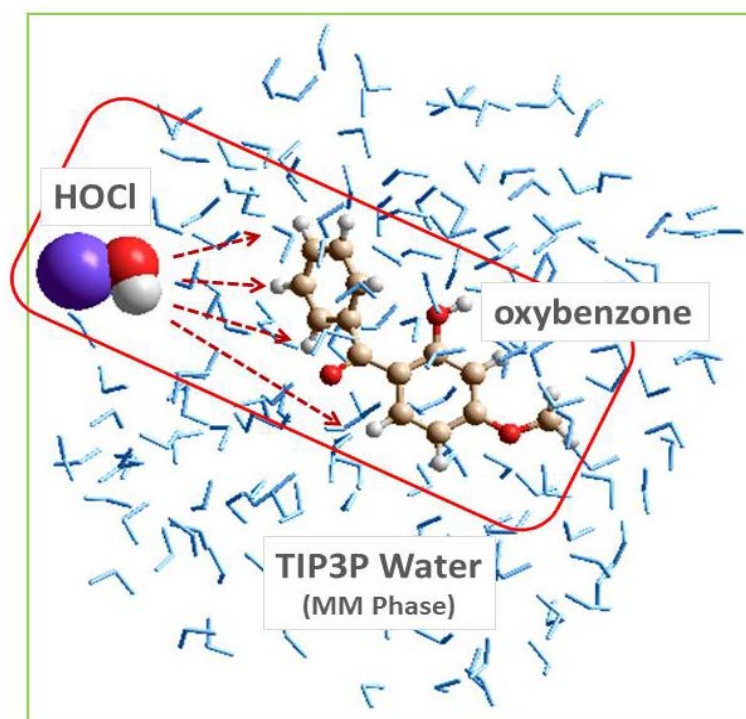

Figure 1. General arrangement of water and HOCl and OxBZ reactant species inside the nano-scale solvation cage at t=0ps just prior to invoking N_{eq}FMD collision. The red box indicates the approximate region treated by the QM method (RM1). Note that some TIP3P water molecules were routinely included in the QM calculation during the early (QR1 cycle) part of the collision trajectory (see Figure 2). See text for other details.

semiempirical calculation method, *i.e.,* RM1/UHF [31] and/or an *ab initio* calculation using the 6-31G** polarizable basis set (spin multiplicity = 3). The QM calculations were also used to assign partial atomic charges to all atoms in the systems. Optimization convergence criteria were typically set at 0.1-0.01 kcal/mol-Å depending on the length of the calculation and available CPU resources. Following the QM optimization calculations, the structures were further refined by performing several additional alternating cycles of semiempirical (or *ab initio*) calculations and optimization by the Amber99 force field using standard Coulomb electrostatics, a switched cutoff and distance-dependent dielectric for the non-solvated conditions. Electrostatic and Van der Waals 1-4 scale factors were each set at their default values of 0.5 for the Amber force field. In a later step described below, TIP3P water models [32] were used to solvate the reactant molecules in preparation for carrying out the N_{eq}FMD simulations.

Table 1. Typical N_{eq}FMD settings used in this study.

RXN Parameter	Value	Notes
semiempirical QM method	RM1	parameterized for all elements in this study
SCF convergence	0.01	
SCF iterations	50	
UHF or RHF	UHF	UHF = unrestricted Hartree-Fock
spin multiplicity	3	1 or 3 for closed shell systems; 2 for open shell
net system charge	0e	total charge of molecular system
DIIS invoked	yes	acceleration ofSCF convergence
mechanics force field	Amber99	Ɛ=1; 1-4 scale factors: estatic = 0.5; VDW = 0.5
assigned velocity (initial)	75-90 Å/ps	velocity vector of HOCl at t = 0ps
number of QR cycles	5	water optimization between each QR cycle
MD run time regression coefficient	0.1	successive QR cycle run times reduced by 0.1
MD time step regression coefficient	0.1	successive QR cycle time steps reduced by 0.1
initial MD time step	0.5fs	floor = 0.25 fs
initial MD run time per QR	0.075ps	floor = 0.025 ps
dynamics temperature cutoff	6000°K	temperature above which rxn is terminated
include water in QR1 cycle	yes	included water treated by QM (can enter rxn)
water distance cutoff	5Å	distance from HOCl and/or OxBZ
pre-collision convergence	10 kcal/mol-Å	rough RM1 optimization prior to each QR cycle
maximum OxBZ rotation	72°	random independent rotation about XYZ axes
maximum HOCl rotation	360°	random independent rotation about XYZ axes
OxBZ targeted atoms	1, 3, 10, 15	random selection of target atom
target atoms: other molecules	COM	COM = center of mass
max rotation: other targets (*e.g.,* aniline)	360°	random rotation about XYZ axes

3.2 Description of N_{eq}FMD Algorithm and Simulations Protocols: Reactive molecular collisions were managed according to a novel N_{eq}FMD algorithm [30] that was scripted using the Tool Command Language and Toolkit (https://www.tcl.tk/software/tcltk/). Reactants were introduced into a non-periodic "nano-solvation cage" (NSC) comprising ~100-200 explicit TIP3P water molecules adjusted to a density of ~1.0g/cc at STP (see Figures 1 and 2). Because solvent can influence reaction outcomes by dipole interactions, steric hindrance of prescribed reactant trajectories, or by directly entering the reaction pathway itself, the N_{eq}FMD algorithm incorporated provisions to allow water proximal to one or both reactants (e.g., within a 5Å shell radius) to enter into the RM1-contolled reaction coordinate. Reactants were initially separated
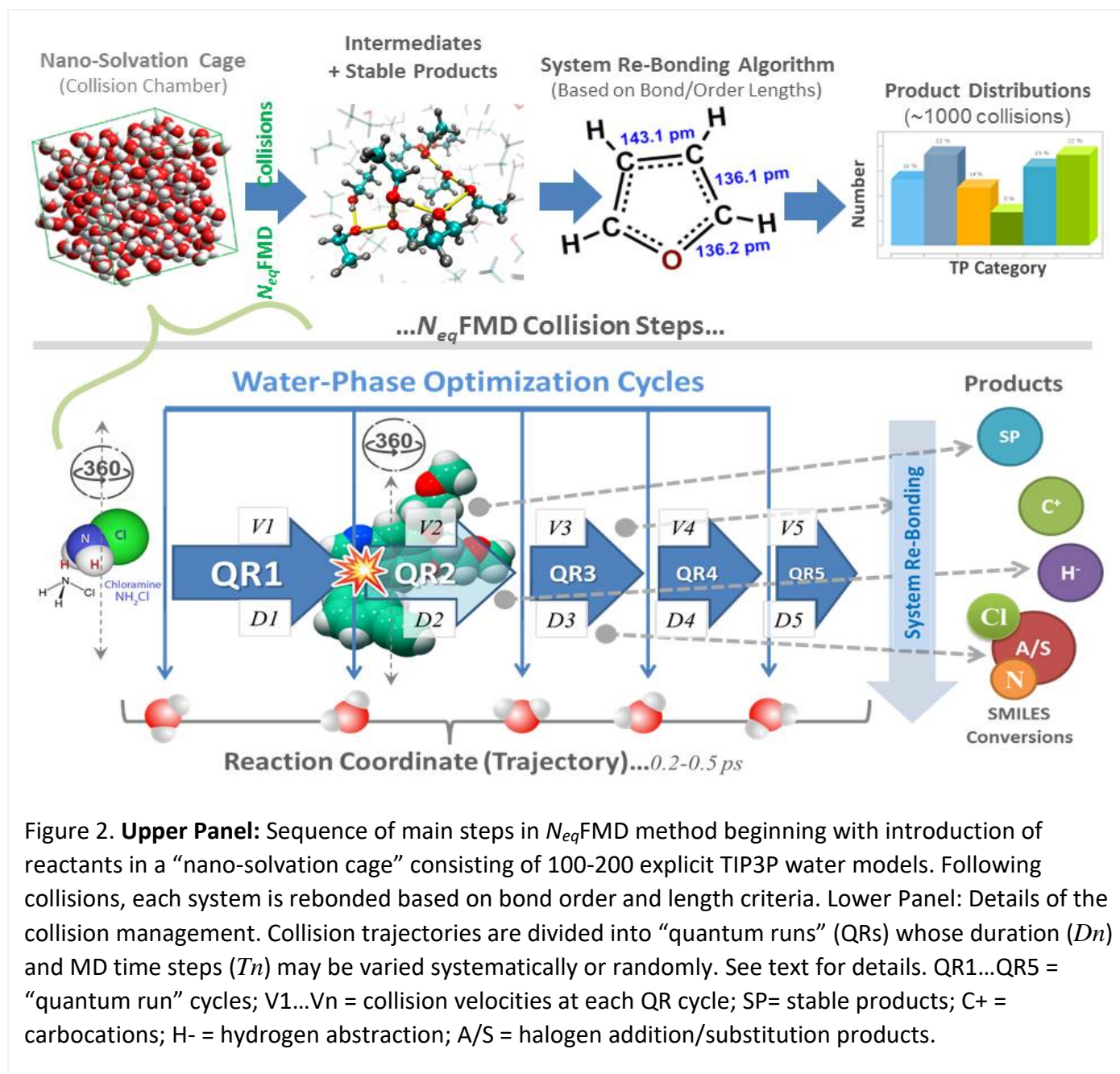

Figure 2. **Upper Panel:** Sequence of main steps in N_{eq}FMD method beginning with introduction of reactants in a "nano-solvation cage" consisting of 100-200 explicit TIP3P water models. Following collisions, each system is rebonded based on bond order and length criteria. Lower Panel: Details of the collision management. Collision trajectories are divided into "quantum runs" (QRs) whose duration (Dn) and MD time steps (Tn) may be varied systematically or randomly. See text for details. QR1…QR5 = "quantum run" cycles; V1…Vn = collision velocities at each QR cycle; SP= stable products; C+ = carbocations; H- = hydrogen abstraction; A/S = halogen addition/substitution products.

from one another by approximately 8-12Å and independently randomly rotated on their XYZ axes to scramble their pre-collision orientations. Because the OxBZ molecule was non-spheroidal and asymmetric (axial ratio >2.0), the maximum allowable rotation along any given axis was restricted to <=72 degrees. This amount of rotational freedom was sufficient to permit collisions with the HOCL molecule that were unbiased by the OxBZ reactant orientation, but not so great as to leave any portion of the rotated OxBZ extending outside the NSC. Orientation bias was further suppressed by randomly targeting four atom centers distributed across the major axis of the OxBZ molecule. These atoms included 1, 3, 10 and 15 (see OxBZ atom numbering scheme below, Figure 5); and at the beginning of each collision, immediately following axial rotations, only one of these atoms was randomly selected as the collision target for HOCl. Typical adjustable variables and settings used in the N_{eq}FMD simulations are summarized in Table 1.

Following introduction of the reactant species, the complete system (*i.e.*, water + reactants) was energy minimized to <0.1 kcal/mol-Å using the AMBER99 force field with a constant non-scaled dielectric (Ɛ = 80). Water molecules >5Å distant from the HOCl center-of-mass were designated as "mechanical atoms", which rendered them immobilized (*i.e.*, frozen or tethered) and only accessible in the SCF (MO) calculations as an electrostatic background. The HOCl molecule was subsequently accelerated toward the target organic compound at the user-specified velocity (75-90Å/ps in this study).

To help avoid excessive (and unstable) repulsive energy gradients over the reaction coordinate and reduce the likelihood of collapsing the SCF calculations, the trajectory was split into 4 to 6 discrete "quantum runs" (QRs) controlled by the RM1 method using a spin multiplicity of 3 and "Pulay mixing", *i.e.*, direct inversion of the iterative subspace [33, 34] to improve energy convergence. Each QR corresponded to one segment of the total collision trajectory. To further relieve excessive interaction potentials, reactants were briefly re-optimized immediately prior to each QR cycle using the RM1 method with a maximum of 10 iterations or a convergence value of 10 kcal/mol-Å. At the end of each QR cycle the reacting species were "frozen" (tethered) and the water phase was re-optimized by a suitable Newtonian force field (typically AMBER99) to permit adaptation of the TIP3P water to the updated nuclear positions of the reactants. Following water re-optimization, the aqueous phase was again tethered and the reactants were allowed to continue (*i.e.*, restart using stored velocities from the previous QR cycle) along their pre-established collision trajectories and adapt to the immobilized water background, which served as a perturbation on the RM1 electronic (*i.e., clamped-nucleus*) Hamiltonian (**H**$_{elec}$). The collision velocity ($V_1...V_n$, *where n = the QR cycle number*), duration ($D_1...D_n$) of each QR cycle, and the MD time step ($TS_1...TS_n$) were user-adjustable parameters and could be autonomously decremented by ~10-15% per QR cycle until a specified minimum "floor" was reached as the reactants approached one another, ostensibly to allow more time for reactant reorientation and relaxation of repulsive non-bonded (Lennard-Jones + Coulomb) interactions. Standard initial velocity and QR duration in this study were usually set at ~75-90

Å/ps and ~0.05-0.075 ps, respectively, using a 0.5 fs MD time step, resulting in a total reaction time of approximately 0.25-0.5 ps. Reaction durations could vary depending on reactant chemistries (see below). Typically several N_{eq}FMD test runs were performed to calibrate the time of reactant "impact" (RIT), *i.e.*, the point where the system reached a maximum "activation" (strain) potential due to molecular orbital distortions. The RIT was typically adjusted to approximately coincide with the end of QR1 or very early in the QR2 cycle. This QM/MM cycling process was continued for each collision until the last QR cycle was completed, at which time the molecular system and trajectory files were saved for subsequent system rebonding and analysis (see below).

Choice of a semiempirical quantum-chemistry method (RM1) to dynamically emulate small-organic reactive collisions in an aqueous background was based primarily on the large size of the molecular systems and applicability to the atom types involved. The nano-solvation collision cages typically were comprised of one organic molecule (*e.g.*, OxBZ) + 100-200 explicit TIP3P water molecules + a single oxidant species, *e.g.*, HOCl, H_2NCl or O_3. Such systems were too large to perform iterative MD simulations over pragmatic time scales using higher levels of QM theory, including small-basis-set *ab initio* or DFT protocols. The RM1 method was also well parameterized for the main group organic/inorganic atom types encountered in this study (C, H, O, N, P, S, Cl). Although some systematic inaccuracies and unpredictability is to be expected in the use of RM1 (or other semi-empirical methods) to emulate chemical bonding in small organic systems (namely due to the lack of explicit electron correlation), the goal here was to *rapidly* generate a distribution of *potential* collision outcomes that could be statistically searched for reasonable reaction patterns that could be subsequently compared to and verified against published experimental data. Finally, it is noteworthy that many modern semiempirical methods, including RM1 and others that have undergone empirical corrections (i.e., reparameterization) and formal extensions, provide improved conformational energies, heats of formation, and hydrogen-bond enthalpies that approach those of *ab initio* or DFT calculations [35-38].
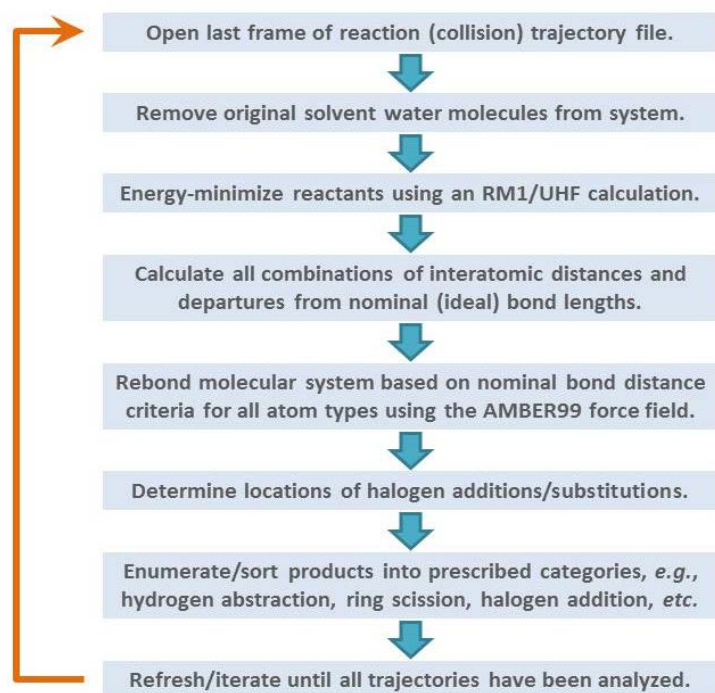

Figure 3. Outline of main steps involved in the system rebonding algorithm. See text for details.

3.3 System Re-Bonding Algorithm and Collision Product Identification: Following completion of all collisions in a series, a second custom algorithm (also encoded in Tcl/Tk) was invoked to re-bond the molecular system based on the magnitude of departure of calculated bond distances from their thermodynamically ideal (normal mode) values (see Figure 3). Bonding and non-bonding distance criteria were independently user-adjustable variables and their values were established based on prior RM1 studies (data not presented). Initial QR velocities and reaction durations depended to some extent on the chemical nature of the reacting species; thus, numerous N_{eq}FMD test runs were conducted for each reactant pair to establish the initial N_{eq}FMD run parameters. Based on their mass, charge, elemental composition, atomic coordination, and other factors the re-bonding script automatically scanned, enumerated and categorized all reaction products regardless of their chemical stability, *e.g.*, hydrogen-abstracted, halogen substituted species, arenium ions and so forth. The combined (*i.e.*, the N_{eq}FMD + rebonding) algorithms were iterated over multiple independent collision events (typically >1000 in this study) for each reactant pair to generate a frequency distribution of 1st-generation reaction products. Finally, because all parameters for each reaction are saved, it is possible to reproduce any given reaction for later detailed analysis.

4.0 Results and Discussion:

4.1 Model Compound Properties: Semiempirical (RM1 method) and *ab initio* (6-31G** basis set) calculated groundstate orbital energies, atomic partial charges and other structural properties for the HOCl and OxBZ models used in this study are summarized in Figures 4 and 5, respectively. The HOCl (RM1/UHF) model used in this study was in partial agreement with experimental and calculated electronic and structural data for this compound, as cited in the Computational Chemistry Comparison and Benchmark DataBase (http://cccbdb.nist.gov/exp2x.asp?casno=7790923) maintained by the US National Institute of Standards and Technology (NIST; https://www.nist.gov/). The RM1-computed bond lengths (O-H and O-Cl) and H-O-Cl angle were in good agreement with experimental values reported by NIST, although the *ab-initio* (6-31G**) calculated heat of formation (-20.98 kcal/mol) was substantially less than the reported experimental value of -74.5 kcal/mol. The *ab-initio* computed partial atomic charge on the oxygen atom of -0.592e was significantly less than the RM1 computed charge of -0.176e. There was a similarly discrepancy with respect to the assigned charges on the chlorine atom (RM1 = -0.04e; *ab initio* = +0.212e). Despite the generally "softer" RM1 partial charges, the semi-empirical method yielded a dipole moment of 1.507 D, which was in reasonable agreement with the experimental value of 1.631 D.

RM1/UHF calculations of OxBZ indicated a strongly electronically polarized molecule (2.169 D, calculated by RM1) with substantially greater electron density associated with the HOMO orbital of the methoxy-substituted ring (see Figure 5). Calculation of the of the HOMO orbital energy yielded a groundstate energy of about -8.26428 kcal for the *alpha*-spin electron and -8.92662 kcal for the *beta*-occupancy electron. Most of the HOMO electron density (Ψ^2) was distributed over atoms 3 (*ipso* to the –OCH$_3$ group), 4 (*ortho*) and 8 (*ortho*) in the methoxy-
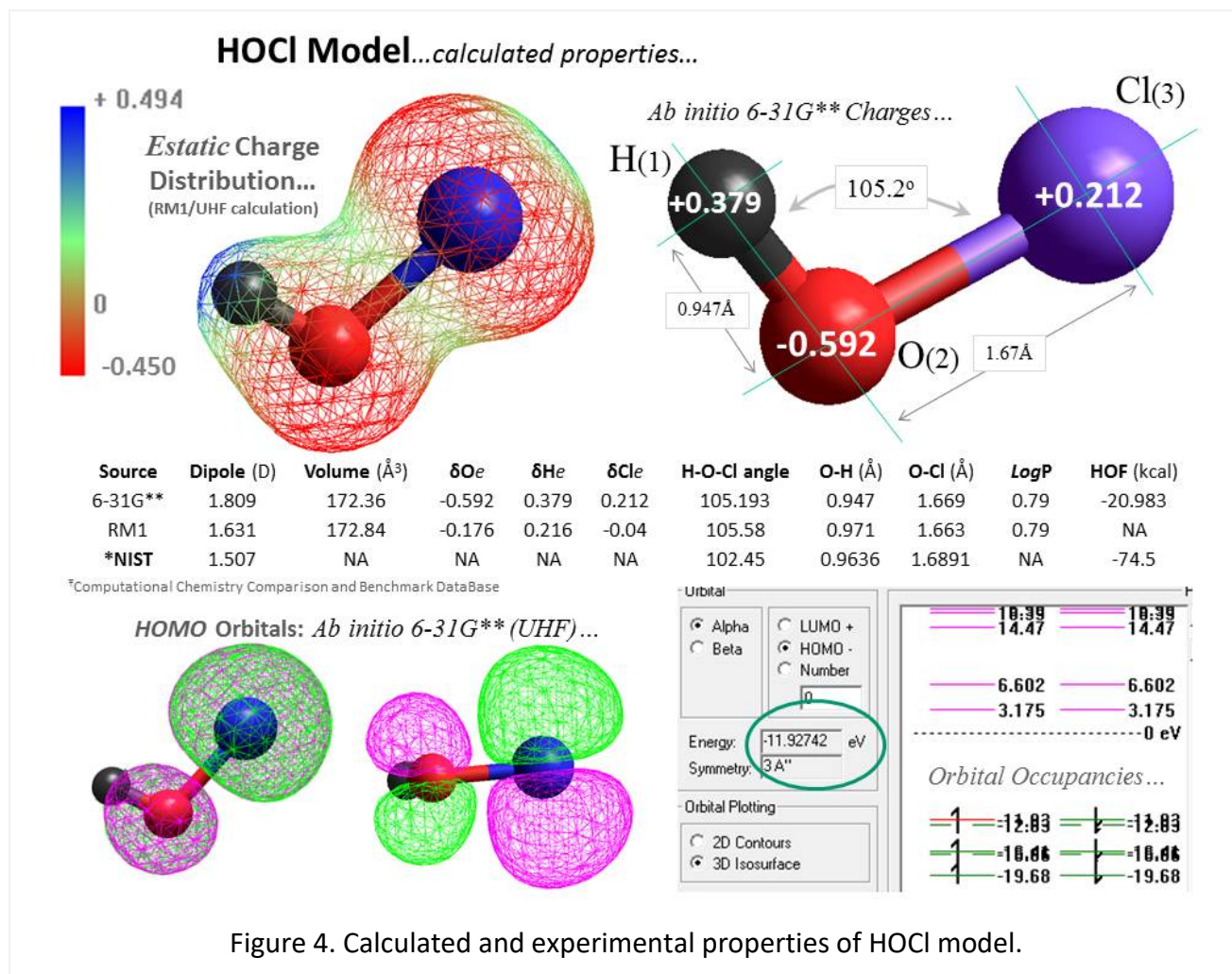
Figure 4. Calculated and experimental properties of HOCl model.

substituted aromatic ring. Strong HOMO orbital density was also associated with oxygen atom 12 comprising the carbonyl bond linking the two aromatic rings.

4.2 Regioselectivity of OxBZ Halogen Addition/Substitution in OxBZ: About 25% of N_{eq}FMD collisions resulted in chlorine addition or substitution TPs, ostensibly resulting from electrophilic attack at preferred atom centers associated with the conjoined aromatic rings (see Figures 6 and 7). Halogen addition/substitution occurrence was highly asymmetrically distributed over the OxBZ target molecule with an approximate 2-fold greater frequency of halogen addition observed in the electron-rich methoxy ring. This observation is in accordance with the higher observed Ψ^2 HOMO density of the methoxy ring compared to the unsubstituted benzene ring. Enhanced methoxy-ring reactivity also correlates favorably with the expected influences of the -OH and –OCH$_3$ activating (i.e., electron-donating) groups, both of which are moderately strong *ortho/para* directing substituents.

In contrast to ring activation by the hydroxy and methoxy groups, the electron-withdrawing

carbonyl bond (--$\overset{\overset{\displaystyle O}{\|}}{C}$-R-) adjoining the two aromatic rings is a moderate deactivating group with a

Figure 5. RM1 semiempirical calculated properties for oxybenzone.
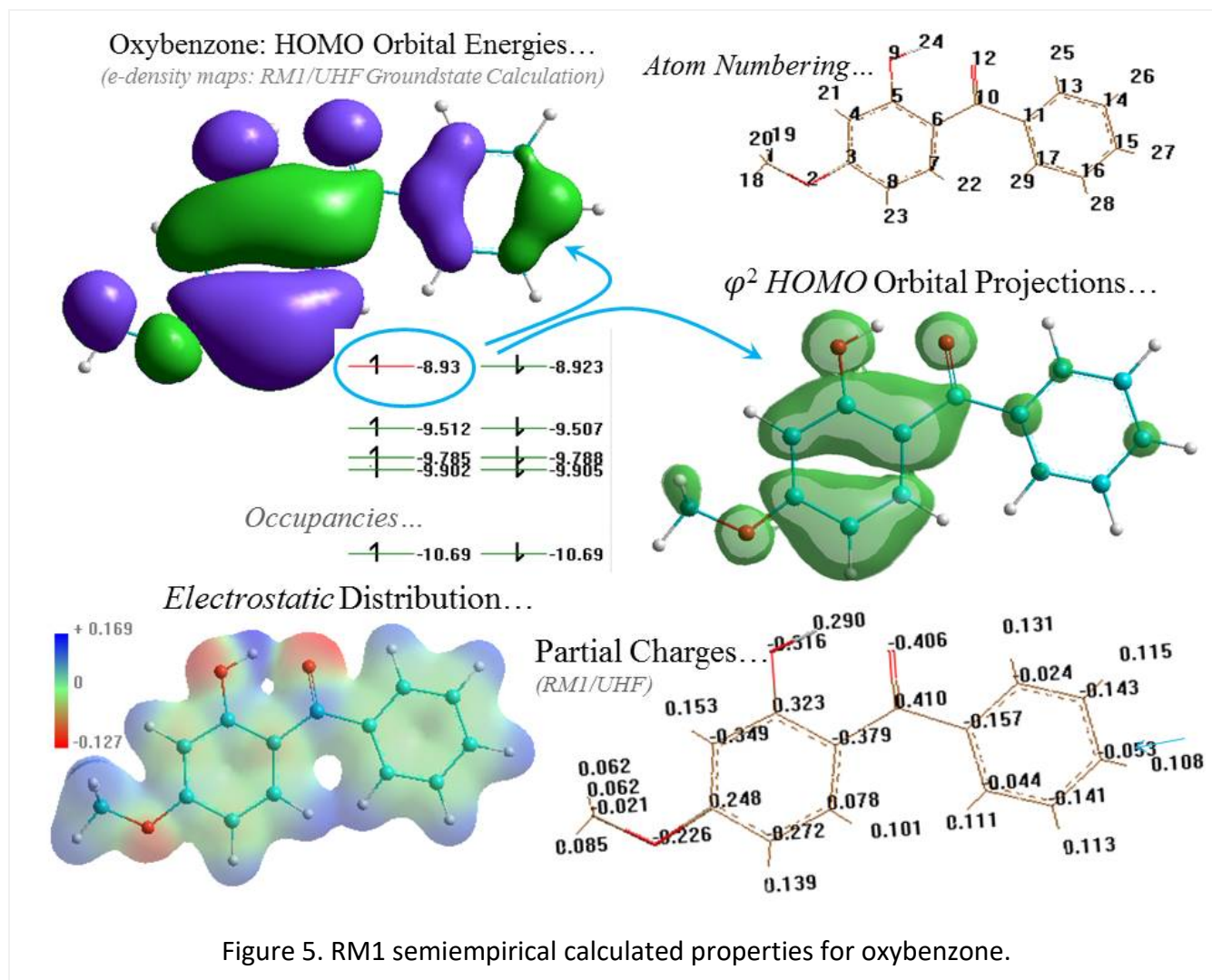
meta-directing influence, which probably contributed to the overall lower reactivity of the benzene ring. The elevated chlorine addition frequency noted at atom 14 in the benzene ring also appears to be consistent with the *meta*-directing influence of the carbonyl group. Based on these observations, the N_{eq}FMD method appears to be in reasonable qualitative agreement with what would be expected based on the known activating and deactivating influences of the OxBZ substituent groups.

Both the hydroxy and methoxy substituents would be expected to complement one another to possibly reinforce their *ortho-para* directing effects and increase electrophilic addition/substitution at methoxy-ring atoms 4, 6 and 8 (see Figure 6). In contrast, repressed halogen attack would be expected at methoxy-ring atoms 3, 5, and 7. While the expected enhancement of chlorine addition was indeed observed at atoms 4 and 8, little or no enhancement was recorded at atom 6 located *para* to the methoxy group and *ortho* to the –OH group. A plausible explanation for reduced halogen addition at atom 6 is that reactivity at this
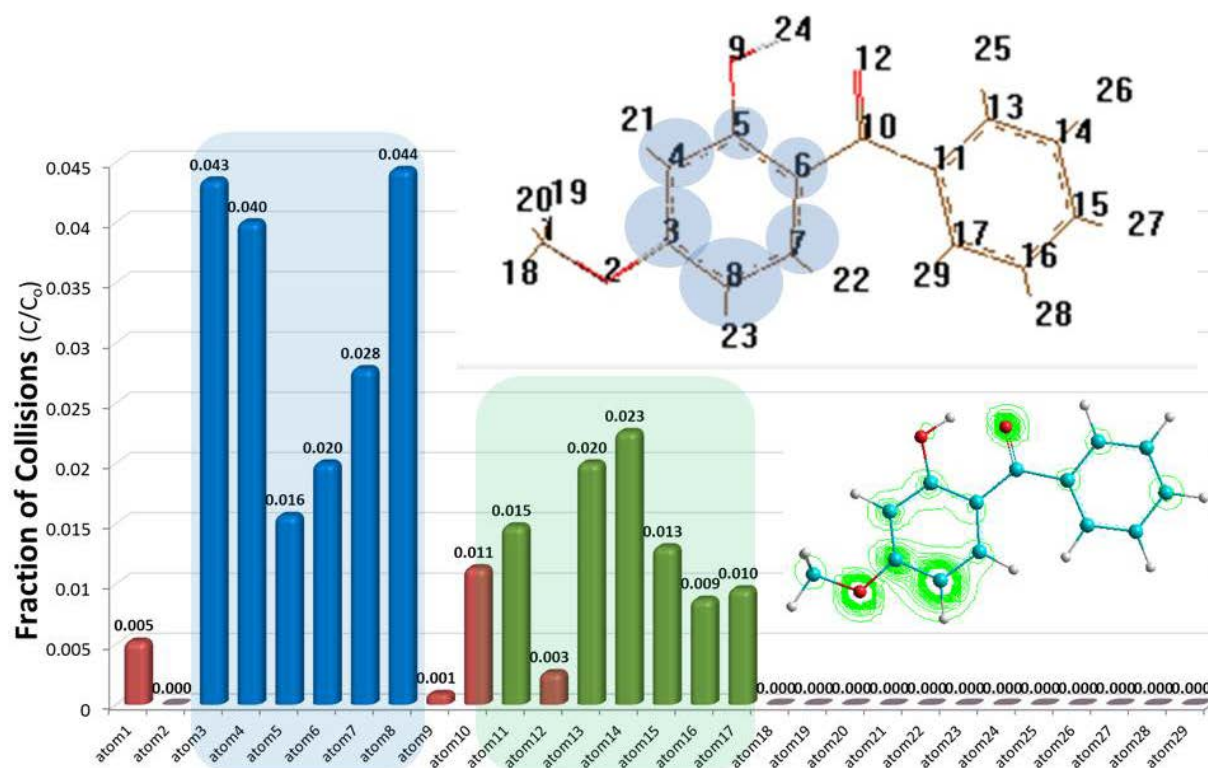
Figure 6. Frequency of chlorine addition/substitution in the N_{eq}FMD simulation over the 29 atoms comprising OxBZ. Note the methoxy ring (blue bars) had about 2x more halogen additions compared to the benzene ring (green bars). Areas of blue circles are approximate the degree of halogen addition at those atom locations. Although halogen addition at the methoxy *ipso* position (C3) was unexpectedly high, it was correlated with elevated HOMO Ψ^2 electron density distribution at this position (inset). The carbonyl bond likely contributed to deactivation of: (1) the unsubstituted benzene ring, and (2) methoxy carbon atom 6 located *ortho* to the –OH group and *para* to the methoxy group.

locus may have been partially curtailed by the *meta*-directing/deactivating influence of the adjacent carbonyl bond.

Interestingly, a heightened rate of chlorine addition was observed at atom 3 in the *ipso* position relative to the methoxy group, which controverted the positive partial atomic charge at this location (+0.248e). While it is possible that the enhanced *ipso* halogen addition was artefactual in nature (*e.g.*, resulting from inadequate handling by RM1 of the oxygen lone pairs in the alkoxy –OCH₃ group), this result was nevertheless correlated with elevated HOMO (frontier) orbital electron density (Ψ^2) mapped at this location and the adjacent *ortho* positions, as revealed by semiempirical RM1/UHF (and *ab initio* 6-31G**) calculations on the optimized parent OxBZ compound (see lower-right inset in Figure 6).

Ipso halogen addition may have also been positively influenced (*i.e.*, promoted) by sterically--induced underestimation of hyperconjugative effects involving the OxBZ methoxy group. Hyperconjugation is known to occur in methoxy groups when favorable alignment occurs between the π-orbital of an oxygen lone pair and one of the adjoining C-H σ* anti-bonding orbitals [39, 40]. Under normal circumstances, hyperconjugation deferentially facilitates delocalization of electron density from the π-orbital of the oxygen lone-pair into the methyl moiety, which effectively shunts charge density away from the aromatic ring rendering it less susceptible to electrophilic attack, particularly at the *ipso* position. However, hyperconjugation depends critically on the conformational space occupied by the methoxy group [39]; and in the relatively high-velocity collision dynamics imposed on the reacting species in this study, the methoxy conformations were oftentimes highly strained sterically. It is speculated that such departure from an optimized –OCH$_3$ geometry over the collision trajectories may have led to severe misalignment of the -O-C-H- σ*-π bond. This in turn could lead to greater electron density being delocalized into the aromatic ring at the *ipso* carbon, which would ultimately be manifested as an enhancement of electrophilic attack at this location.

Ipso additions/substitutions typically occur under specialized circumstances, such as certain nitration reactions [41] or enzyme-catalyzed hydroxylation of *para*-cresol and related aromatic phenols by cytochrome P450 [42]. In the later situation, substituent elimination is accompanied with *ipso* substitution by an oxygen atom of the active species, and there is a requirement for a hydroxyl group at the *para*-position to the leaving group. *Ipso*-mediated hydroxylation reactions have also been reported in the enzyme catalyzed biodegradation of *bis*-phenol-A (which has a bi-phenolic structure resembling that of OxBZ) and nonylphenols by *Sphingomonas* [43]. The authors reported that subsequent to *ipso* hydroxylation, various molecular rearrangements took place consistent with the formation of transient *pseudo*-stabilized carbocation intermediates. A similar mechanism involving *ipso* ring hydroxylation at the site of the substituent has been described by Gabriel *et al.* [44]. Fischer and Henderson [45] reported bromination of *para*-cresol via a mechanism involving halogen addition *ipso* to the 2-methyl group followed by migration of the bromine to the adjacent 3-position.

Similar *ipso* substitution mechanisms to those described above were observed in the N_{eq}FMD simulations conducted in this study (see Section 4.7 below). For example, reactions 115 and 885 resulted in the release of a formaldehyde *di*-radical (•CH$_2$O•) leaving group following *ipso* hydroxylation or chlorination, respectively. The former reaction yielded the stable product *di*-hydroxybenzophenone while the later resulted in formation of *chloro*-hydroxybenzophenone, neither of which has been previously reported in experimental studies. Similarly, at least five reactions (#'s 95, 225, 577, 681, 976) involved hydroxylation at the methoxy *ipso* carbon coupled with cleavage of the O-CH$_3$ bond to yield a chloromethane product + *di*-hydroxybenzophenone.

Formation of *ipso* halogenated TPs in OxBZ chlorination reactions have not been reported by others [16-20], but this may have been due to the transient nature of such quasi-stable

intermediates and the difficulty of their detection. Moreover, because only 1st-generation N_{eq}FMD collision products were captured in this study, it is unknown if the carbocation *ipso* addition TPs might have undergone subsequent structural rearrangements to yield energetically more favorable isomeric forms via resonance delocalization processes.

4.3 Halogen Addition/Substitution in Phenol, Anisole and Aniline: To further evaluate the ability of the N_{eq}FMD method to emulate the activating/directing influences of specific OxBZ substituent groups, the N_{eq}FMD method was applied separately to phenol (1100 collisions) and anisole (1150 collisions), whose single hydroxy and methoxy substitutions, respectively, are known ring-activating (electron-donating) and *ortho/para* directing groups. As an additional test of the ability of N_{eq}FMD simulations to differentiate between the directing/activating
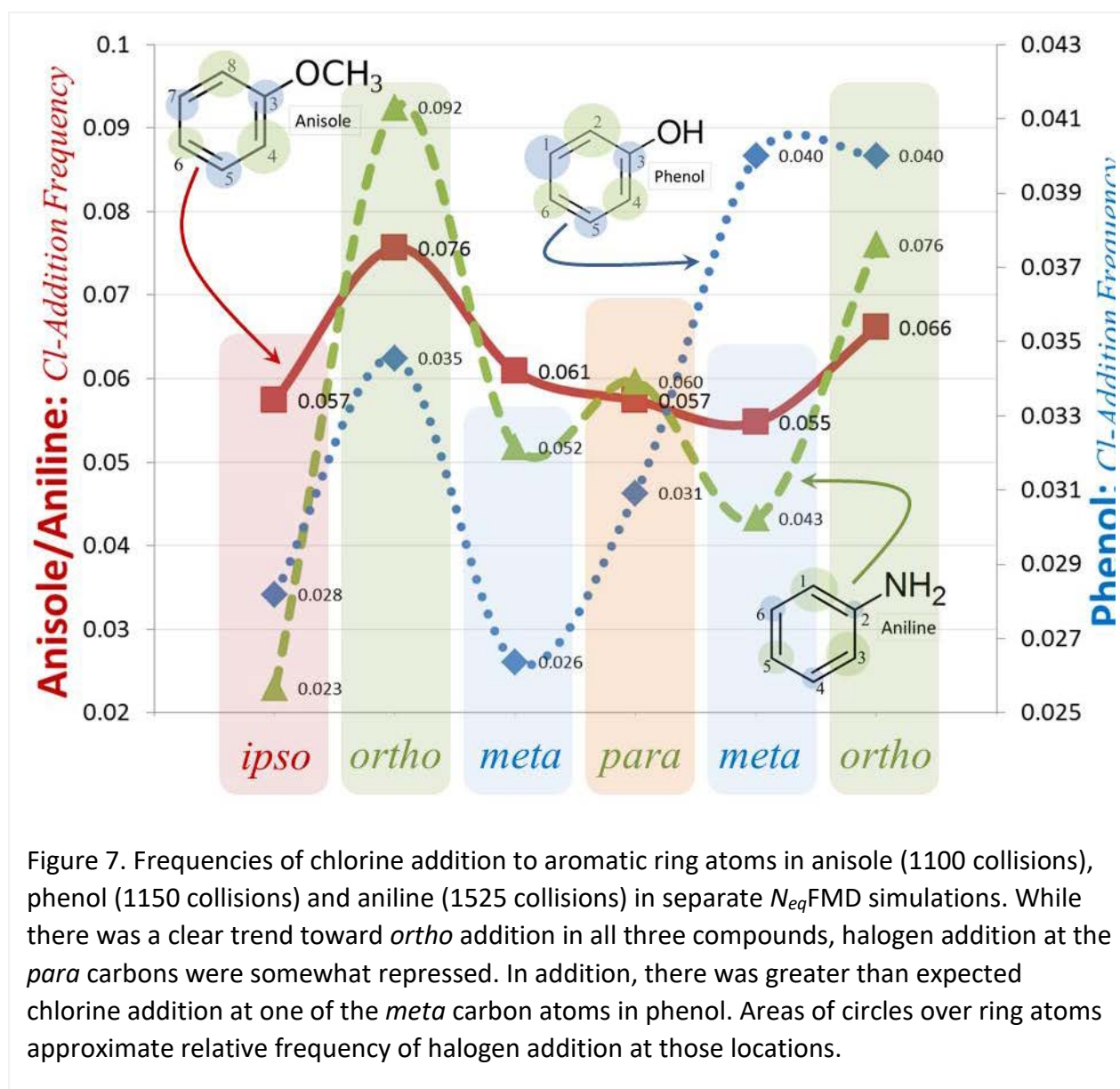

Figure 7. Frequencies of chlorine addition to aromatic ring atoms in anisole (1100 collisions), phenol (1150 collisions) and aniline (1525 collisions) in separate N_{eq}FMD simulations. While there was a clear trend toward *ortho* addition in all three compounds, halogen addition at the *para* carbons were somewhat repressed. In addition, there was greater than expected chlorine addition at one of the *meta* carbon atoms in phenol. Areas of circles over ring atoms approximate relative frequency of halogen addition at those locations.

effects of certain substituent groups (namely –NH$_2$) a third N_{eq}FMD run was included for aniline (1525 collisions).

A summary comparison of the results from these simulations is presented in Figure 7. Inspection of the data suggest the following conclusions: (1) Halogen addition was in general more likely (by about 2-fold) for aniline and anisole as it was for phenol under similar or identical N_{eq}FMD simulation conditions; (2) For all three compounds *ortho*-addition of chlorine was mostly favored over addition at the *ipso*, *para* and *meta* positions. One exception to the later generalization was a comparatively high halogen addition frequency observed for the first *meta*-position of phenol (atom 1).

On strictly quantitative grounds, the later observation stands in contrast to the experimental findings of Ogata *et al.* [46] who reported that the *ortho/para* ratio in the chlorination of phenol and anisole with aqueous NaOCl was about 0.64 and 0.66, respectively, under acidic conditions. However, these authors also reported a strong preference for *ortho*-substitution of phenol at pH 10 (*ortho/para* ratio = 4.3), an observation that is clearly more closely aligned with results from the current N_{eq}FMD simulations. Because the simulations did not explicitly account for pH effects and different forms of chlorine were used in the two studies, it is difficult to rationalize the current modeling results with the findings of Ogata and coworkers [46].

The observed higher reactivity of aniline compared to phenol and anisole in the N_{eq}FMD simulations was in good qualitative agreement with the known experimental behavior of these compounds with regard to their halogen (electrophilic) reactivity. The finding that aniline and anisole exhibited a greater frequency of halogen addition than phenol in the N_{eq}FMD simulations suggests the methoxy and primary amine groups, respectively, were more activating than the hydroxy group. In practice, however, phenol is usually found to be slightly more reactive with halogen species than is anisol. The reduced halogen reactivity of anisole (in practice) presumably results from stabilizing hyperconjugation between the methoxy oxygen π-lone pair(s) and the antibonding σ*-MO of the aligned –C-H bond [40, 47]. In anisole a negative hyperconjugative effect tends to delocalize electron density away from an oxygen lone pair (and into the –C-H σ*-MO) that would otherwise be contributed to the aromatic ring through a π-π resonance mechanism. In phenol, hyperconjugation is absent leaving more electron density available at the oxygen lone pair(s) to be donated to the ring via resonance charge transfer.

It is concluded that some incongruity exists between the N_{eq}FMD modeling results that indicate a somewhat reduced activating influence of the hydroxy substituent in phenol compared to the overall higher reactivities of anisole and aniline. Whereas the basis for this discrepancy is unclear at this time, it is probably not related to an inability of the RM1 method to model hyperconjugation effects in anisole, since these processes are computed with reasonable confidence by similar NDDO semiempirical methods, including PM3 [48]. As described above for OxBZ, a likely source of error in anisole might be excessive (collision-induced) bond vibrational fluctuations during simulations causing poor MO alignments and reduced -OCH$_3$

hyperconjugation, resulting in greater aromatic electron density and a corresponding rise in the probability of halogen attack [40].

The modeling data also indicated that halogen addition preferences, *i.e.*, substituent directing effects, were milder than what might be expected based on experimental reactions between halogens and substituted aromatic compounds [49]. Indeed some repression of halogen addition was evident in the *para* positions of all three compounds; and addition at one of the phenol *meta* positions (atom 1) was inordinately high for unknown reasons. Thus, it may be concluded that overall the *Neq*FMD algorithm, as currently implemented, is in partial qualitative accord with expectations based on experimental observations, but tends to discriminate less strongly than would be observed in practice between the directing effects of certain substituent groups, *e.g.*, the methoxy group.

The divergence from experimental observations may also be attributed in part to relatively "soft" partial atomic charges computed by the RM1/UHF method (*e.g.*, compared to *ab initio* computed charges; see Section 4.1 above), which might diminish polarization effects and dipole interactions with the oxidizing species resulting in weaker directing influences of some substituent groups. A second possibility is that the collision velocities used in the current study were sufficiently high as to partially dampen (*i.e.*, swamp) the effects of higher activation energies associated with less preferred sites of halogen attack. Yet a third possibility could be related to the rather extreme conformational changes that occur in the oxidant and target species during the molecular collisions. Large conformational fluctuations resulting from kinetic transference from the oxidant species would tend to alter and destabilize groundstate MO arrangements in such a manner as to partially scramble and thus weaken the discriminatory influences of substituent groups. Additional studies will need to be undertaken to address these and some other possibilities.

4.4 Occurrence of OxBZ Transformation Products and Intermediates: Despite the limitations described above in the ability of the N_{eq}FMD method to precisely emulate and strongly distinguish between the directing/activating influence of some substituent groups, the algorithm successfully predicted a range of experimentally-verified 1st-generation TPs from a total of 1150 reactive collisions between HOCl and OxBZ dissolved in a TIP3P water nano-solvation cage. These results, which are summarized in Figure 8, indicated that about 15.3% of the 1150 collisions resulted in "failed reactions", *i.e.*, no TPs were observed and the parent reactants remained unchanged. Such failed reactions were principally caused by poor or unfavorable reactant geometries and orientations over the collision trajectories, which effectively nullified any MO rearrangements and subsequent TP formation. Nearly 4% of collisions resulted in "unstable reactions" in which the N_{eq}FMD calculation was automatically terminated when a user-adjustable thermal threshold criterion (see Table 1, above) was exceeded due to an excessive energy gradient for the molecular system.
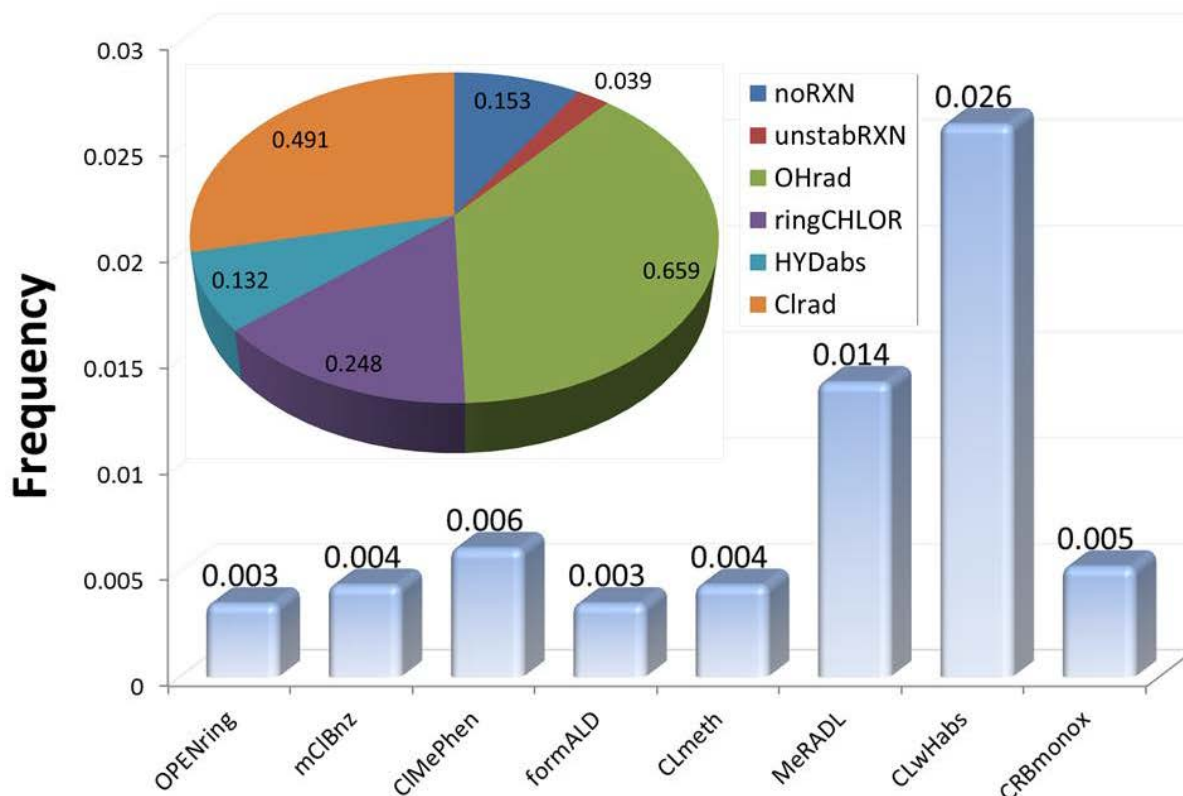
Figure 8. Main reaction product categories observed in the HOCl + OxBZ N_{eq}FMD reaction simulations. Numbers are fraction of occurrences over 1150 collisions. The pie-chart inset indicates occurrences of major TP categories, whereas the bar graph depicts less frequent occurrences of some specific compounds or limited categories. KEY: noRXN=no reaction; unstabRXN=unstable reaction; OHrad=hydroxy radical; ringCHLOR=chlorine addition to a ring; HYDabs=hydrogen abstraction; Clrad=chlorine radical; OPENring=ring scission; mClBnz=mono-chlorobenzene; ClMePhen=chloro-methoxyphenol; formal=formaldehyde; CLmeth=chloromethane; MeRADL=methyl radical; CLwHabs=chlorine addition with hydrogen abstraction; CRBmonox=carbon monoxide.

Among the largest product categories observed were the formation of free hydroxyl (•OH; ~66% of collisions) and chlorine (Cl•; ~49% of collisions) radicals resulting from homolytic dissociation of the HOCl molecule as it approached the OxBZ target compound. In some collisions, chlorine dissociation was observed to occur prior to the point of closest approach to the OzBZ molecule. In these instances, chlorine dissociation was typically initiated by

interaction of HOCl with proximal water molecules lying in the OxBZ collision path that were also treated quantum mechanically in the QR1 cycle.

Chlorine and •OH radical formation was not entirely unexpected since such species are generally produced by homolytic bond scission between two atoms of similar electronegativity (*en*), in this instance between oxygen (*en* = 3.44) and chlorine (*en* = 3.16). In addition the HO-Cl bond energy is known to be comparatively labile (about 48 kcal/mol calculated by RM1 in this study) and it is therefore especially vulnerable to homolytic splitting under the collision conditions used in the N_{eq}FMD simulations (see Table 1, above).
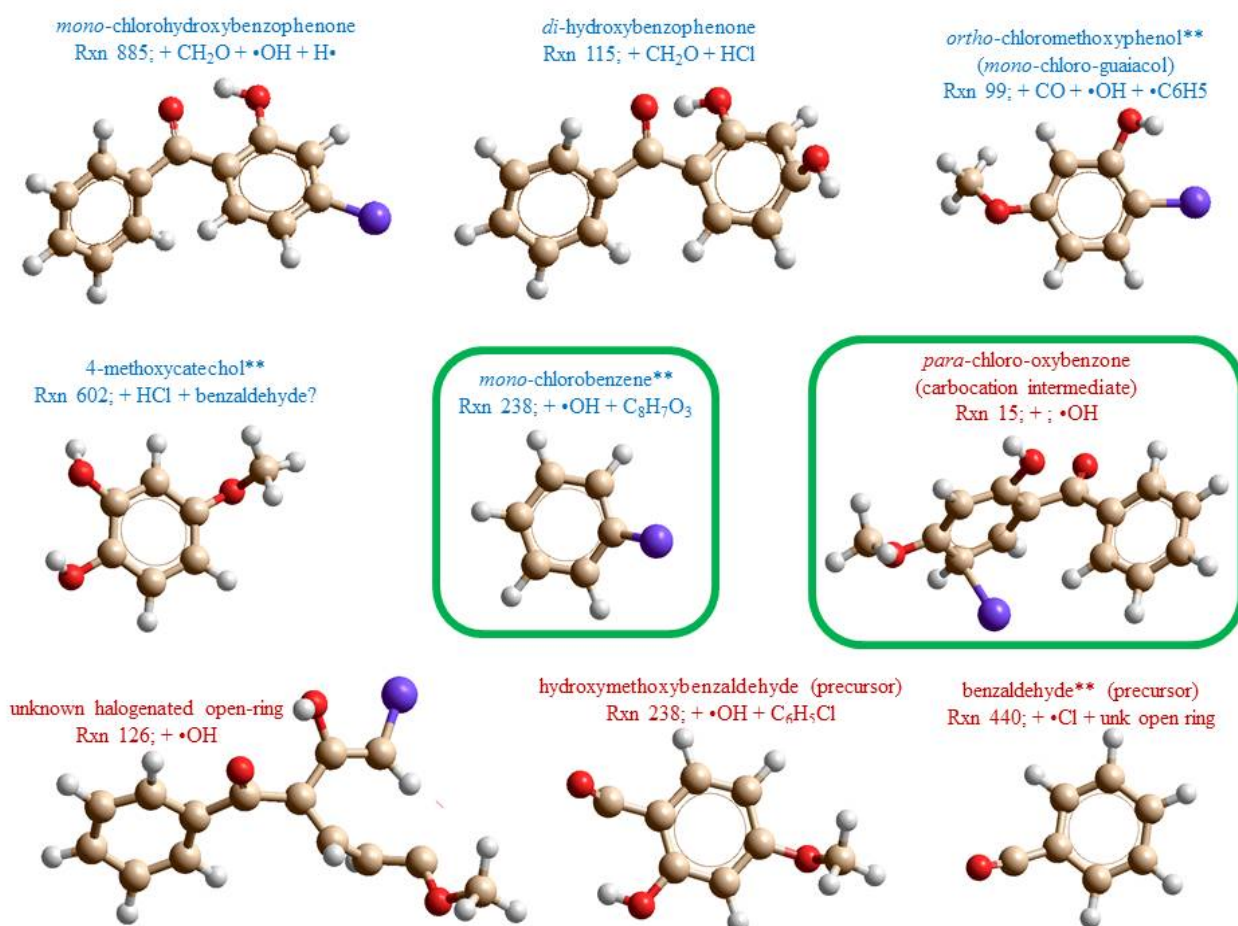

Figure 9. Some specific stable (blue captions) and pseudo-stable (red captions) 1st-generation products observed in the reaction of HOCl with OxBZ. Compounds marked with ** are known human carcinogens. Compounds enclosed in green boxes have been reported in experimental studies. The two benzaldehyde compounds marked as "precursor" (lower right) are radical species that are expected to undergo electron delocalization to yield resonance-stabilized structures.
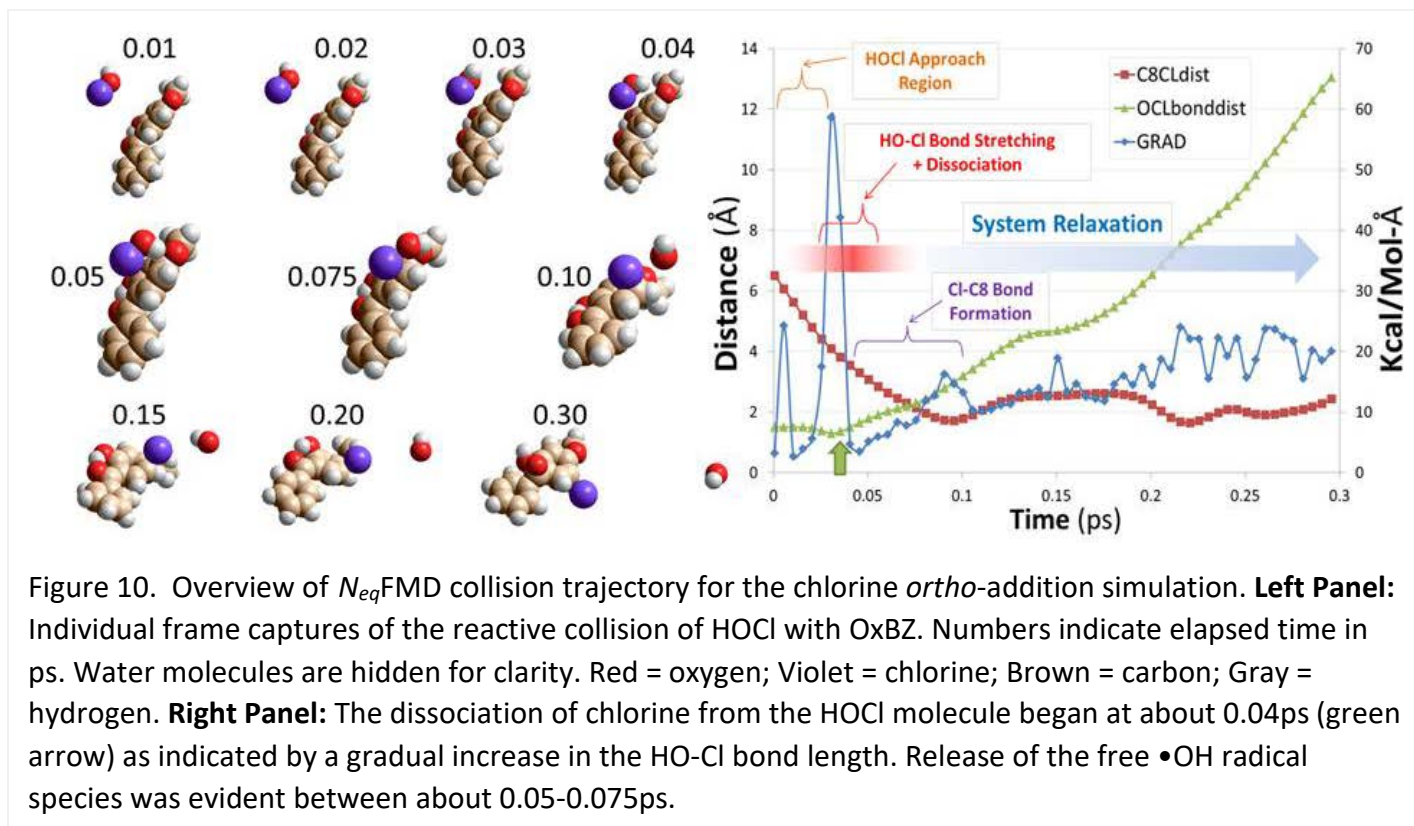
A range of 1st-generation ring-halogenated (~24.8% of collisions) and hydrogen-abstracted (~13.2% of collisions) TPs were observed, including a high frequency of Cl addition at the *ortho* and *ipso* positions relative to the –OCH$_3$ methoxy group, as described above. Mono-halogenated single-ring products resulting from carbonyl bond cleavage, such as *mono*-chlorobenzene (rxn238) and *para*-chloromethoxyphenol (rxn2), were also observed in about 3.1% of collisions. The formation of HCl was also frequently observed in the simulations and typically resulted from the reaction of a hydrogen atom abstracted from the OxBZ parent with a free chlorine radical following homolytic cleavage of the HO-Cl bond. Hydrochloric acid as well as similar or identical monohalogenated TP categories and chlorinated ring-scission products have been observed in OxBZ freshwater chlorination experiments reported by Negreira *et al.* [20] and more recently by Zhang *et al.*[16], as well as in seawater experiments reported by Manasfi *et al.* [50]. Figure 9 provides a summary of specific stable TPs and *pseudo*-stable intermediates that were observed in the current modeling study.

The N_{eq}FMD simulations revealed a number of other TPs that have not been reported or only marginally documented in earlier experimental chlorination studies of OxBZ. Some of these products included relatively rare ring opening reactions (~0.3%), hydroxylation (-OH) additions/substitutions (~8.5%), formaldehyde or formaldehyde *di*-radical precursor (•CH$_2$O•) formation (~0.3%), *mono*-chloromethane (CH$_3$Cl; ~3.1%), and formation of methyl (•CH$_3$; ~1.3%) and methoxide radicals (•CH$_3$O; ~0.3%; Figure 9). The observation of early radical formation suggests that some 2nd-generation TPs (with multiple halogen substitutions) could be readily formed by their further reaction with 1st-generation products and intermediates.

The significant chemical diversity of TPs and intermediates observed in the N_{eq}FMD simulations appears consistent with a scenario in which multiple potential HOCl oxidation routes lead to TP formation. Some of the key routes revealed by the N_{eq}FMD simulations involve: (1) carbonyl bond scission reactions that may or may not be combined with ring halogenation, (2) methoxy group elimination leading to formaldehyde or *mono*-chloromethane formation, (3) facile abstraction of hydrogen from the –OH group, (4) a variety of ring opening reactions, and (5) ring hydroxylation, *e.g.* resulting in formation of 4-methoxycatechol (see Figure 9).

In contrast, experimental studies have generally described a somewhat more limited range of TP formation pathways based on the detection and quantification of a few stable or *pseudo*-stable reaction end products. However, the experimentally observable end products (and intermediates) may not adequately reflect the potential richness of TP formation mechanisms that is suggested by the present modeling study. A possible informative strategy for future experimental research would be to specifically analyze for some of the potential TPs that have been revealed in the current N_{eq}FMD simulations effort.

4.5 Detailed Analysis of Chlorine *Ortho*-Addition/Carbocation Formation: As indicated above, Zhang and coworkers [16] reported a comparatively short-lived (<60 min) semi-stable monochlorinated OxBZ product with a single halogen substitution in the *para* position relative to the –OH side group (*ortho* relative to the –OCH$_3$ methoxy group). This same halogenated TP,

Figure 10. Overview of N_{eq}FMD collision trajectory for the chlorine *ortho*-addition simulation. **Left Panel:** Individual frame captures of the reactive collision of HOCl with OxBZ. Numbers indicate elapsed time in ps. Water molecules are hidden for clarity. Red = oxygen; Violet = chlorine; Brown = carbon; Gray = hydrogen. **Right Panel:** The dissociation of chlorine from the HOCl molecule began at about 0.04ps (green arrow) as indicated by a gradual increase in the HO-Cl bond length. Release of the free •OH radical species was evident between about 0.05-0.075ps.

in its *meta*-stable carbocation intermediate form, was also observed in the N_{eq}FMD simulations. In an effort to shed light on the possible mechanism of this reaction outcome, a more detailed investigation was undertaken of one N_{eq}FMD simulation that resulted in electrophilic chlorine addition to the methoxy-ring C8 carbon atom + release of a free •OH radical. This particular reaction outcome was found to be reproducible across >10 independent N_{eq}FMD trials given the same starting positions and (rotational) orientations of the HOCl and OxBZ molecules (data not presented). An analysis of the time course of the reaction, which is depicted in Figure 10, revealed high initial system strain energy (gradient) as the HOCl approached and underwent a reactive collision with the OxBZ target compound in the vicinity of the methoxy ring. As indicated in the right-hand panel of Figure 10, elongation of the HO-Cl bond first became apparent at about 0.03ps and continued for the duration of the reaction coordinate ($t_{end} = 0.3$ps).

Actual dissociation of the HO-Cl bond occurred between an N_{eq}FMD elapsed time of about 0.04-0.05ps (see Figures 10 and 11) and an HO-Cl bond distance of about 1.5-1.7Å. This bond dissociation event was immediately preceded by a brief collision-induced compression (of about 0.2Å) of the HO-Cl bond that occurred between 0.02 and 0.04ps. The HO-Cl bond compression minimum at about 0.03ps corresponded to the maximum system energy gradient and represents a significant portion of the activation energy for the C8---Cl σ-π conjugation leading to halogen addition to the aromatic ring. This strain energy was abruptly released between about 0.03-0.04ps as the HO-Cl bond underwent dissociation. The HO-Cl bond

dissociation also corresponded to the point of closest approach of the chlorine atom to atom C8 in the methoxy ring, which was located in the *para* position relative to the –OH side group.
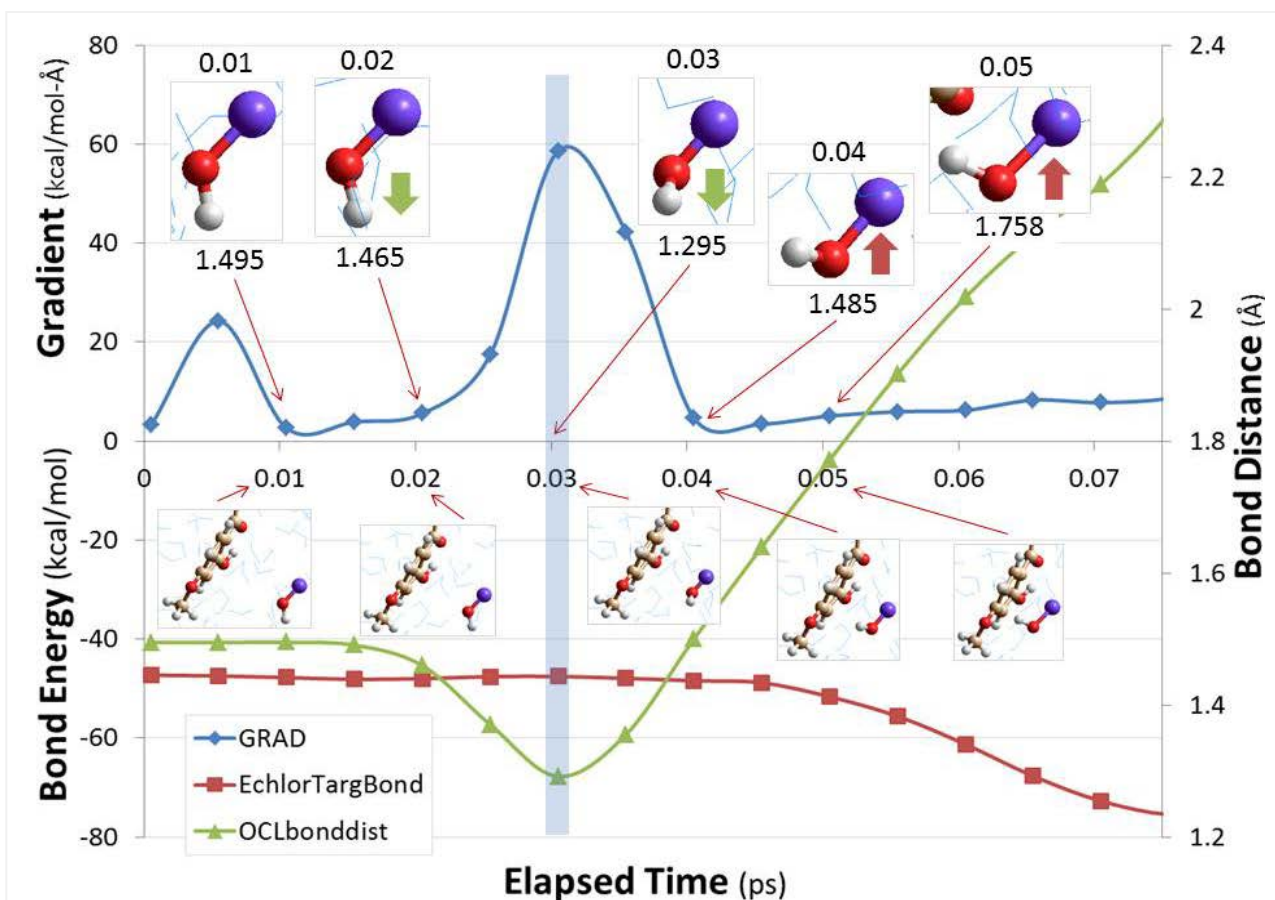

Figure 11. Early part (<0.075ps) of the reaction trajectory yielding the *mono*-chlorinated pseudo-stable OxBZ arenium intermediate. The system gradient (GRAD) increased then decreased during the initial 0.01ps as HOCl approached OxBZ. HO-Cl bond compression between about 0.02-0.03ps (green down arrows) resulted in a sharp spike in strain energy, which was followed by an abrupt decline as the HO-Cl bond underwent stretching and dissociation (red up arrows). This was coupled with nascent Cl-C8 covalent bond formation. Vertical blue bar indicates the point of maximum system strain (GRAD) occurring at the closest approach of the Cl atom to the C8 carbon.

Dissociation of the HO-Cl bond was also accompanied by release of an •OH free radical between about 0.05-0.075ps, after which time the system continued to undergo rapid but comparatively minor conformational changes (i.e., steric relaxation) due to prior conveyance of kinetic energy from the HOCl molecule to the OxBZ target compound. Conformational enthalpies (*ΔH*) calculated by RM1/UHF indicated net downhill thermodynamics for the

formation of a stable halogenated *ortho*-substituted product, assuming eventual loss of the unstable arenium proton in the *ortho* position to the water phase (see Figure 12).
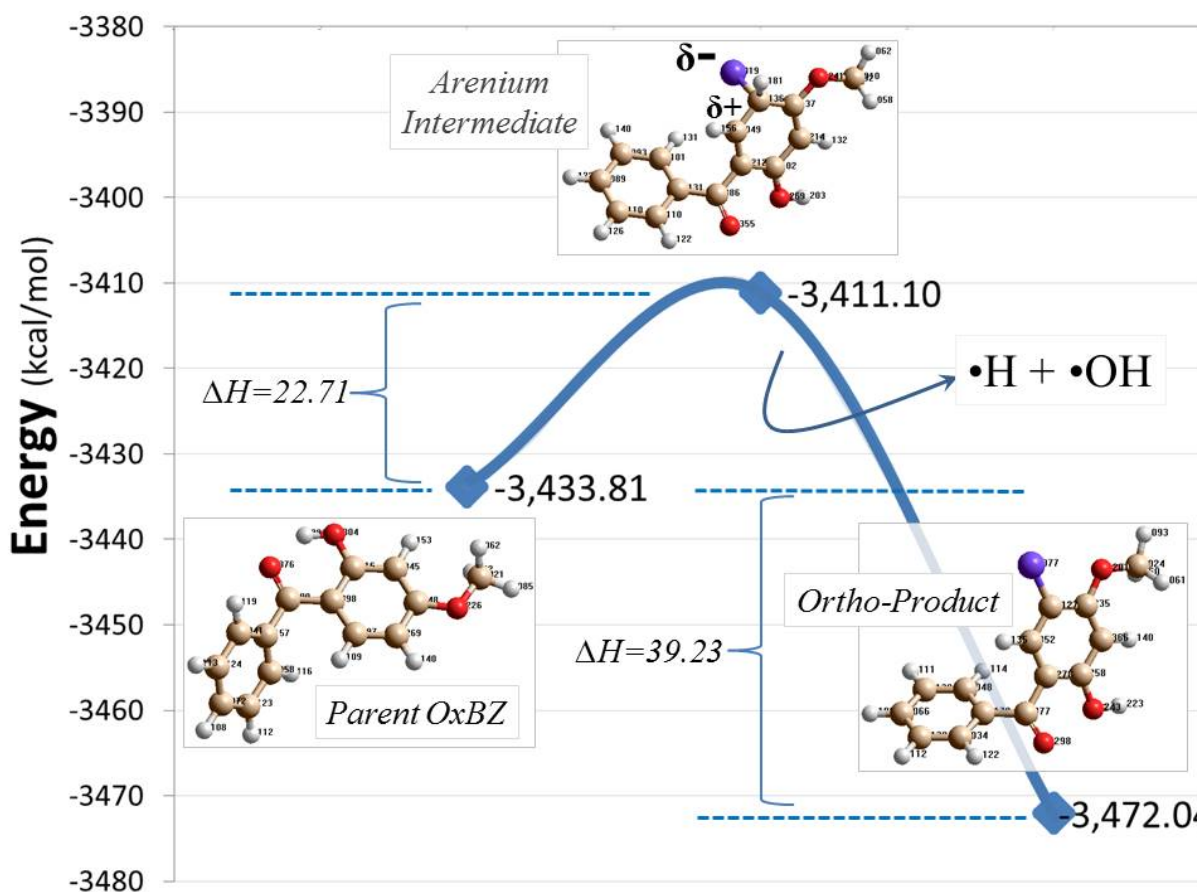

Figure 12. Energies calculated by RM1/UHF for the geometry-optimized parent OxBZ compound, the *meta*-stable carbocation intermediate, and the presumptive *ortho*-substituted product that has been experimentally verified by Negreira *et al.* [20]. Although included in the energy calculation, the HOCl molecule is hidden (for clarity) in the image of the parent compound. Similarly, the free •OH radical is not shown for the intermediate. The calculation for the *ortho*-product included a single water molecule (•H + •OH). In all calculations, the HOCL and •OH molecules were present in their original locations following the N_{eq}FMD simulation.
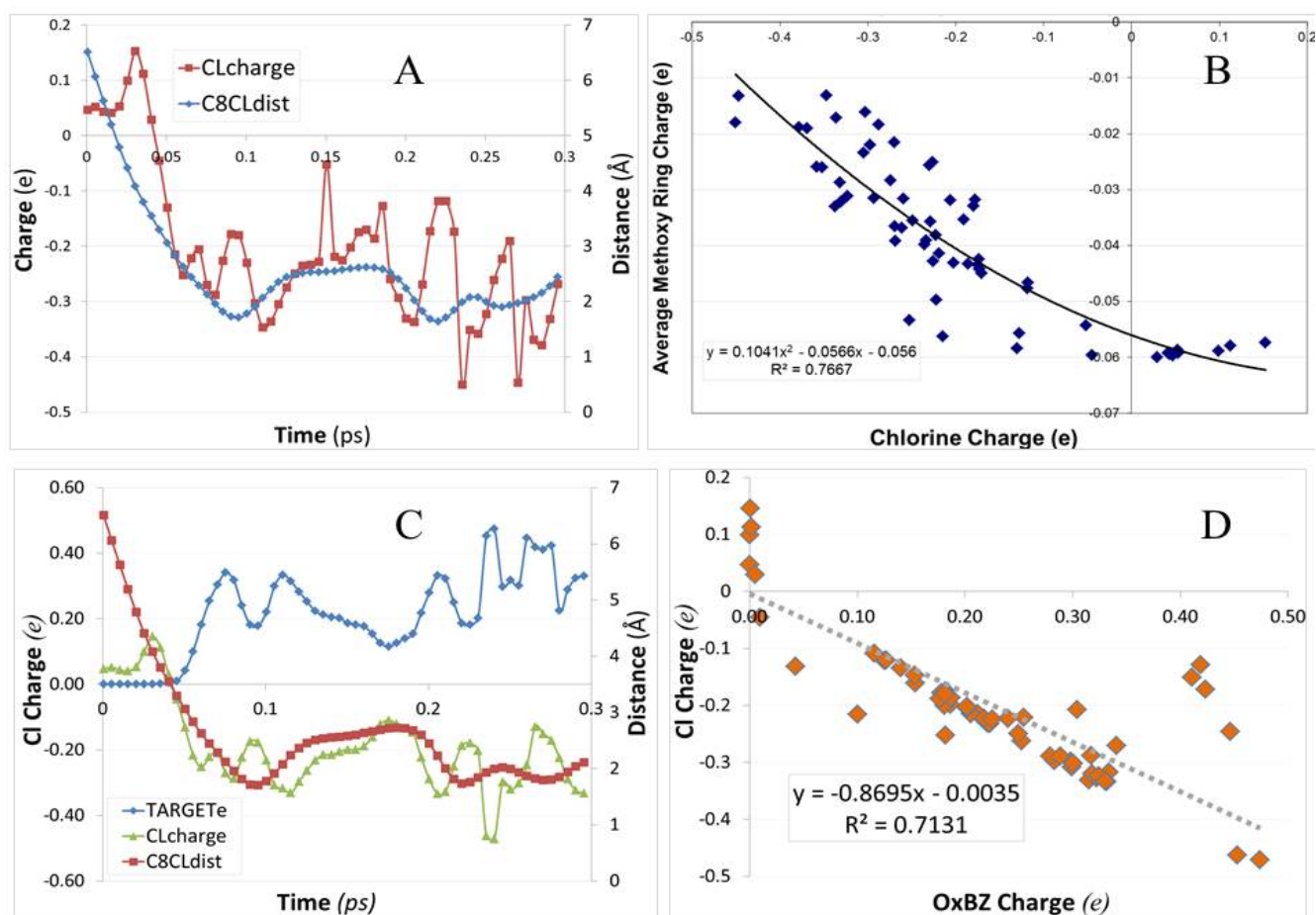
Figure 13. Resonance charge transfer from methoxy-ring aromatic carbon atoms to chlorine during electrophilic addition. **(A)** Partial charge on the chlorine atom (Clcharge) co-plotted with the separation distance between chlorine and carbon atom C8 in the OxBZ methoxy ring as a function of N_{eq}FMD elapsed time. Increased association of these atoms was correlated with deepening of the chlorine atom partial charge. **(B)** Average charge of methoxy-ring carbon atoms as a function of partial atomic charge on the chlorine atom. The inverse relationship is consistent with charge resonance transfer from the methoxy ring to chlorine during collision and nascent Cl-C8 covalent bond formation. **(C)** and **(D)** Inverse relationship between chlorine partial charge and the total charge of the OxBZ target molecule (TARGTe) (*data extracted from a second independent run of the same reaction*).

4.6 Electron Delocalization and Resonance Charge Transfer Effects During Chlorine Addition:
In halogen-mediated electrophilic addition/substitution reactions the partial atomic charge of the halogen species is expected to deepen (*i.e.,* become more negative) as a result of resonance electron withdrawal from the donor atom(s). As shown in Figure 13A such a charge deepening effect of the chlorine atom was in fact observed in the N_{eq}FMD simulations; and this deepening effect was inversely correlated with the separation distance between the chlorine atom and carbon atom C8 in the *ortho*-position of the methoxy aromatic ring.

A similar inverse relationship was observed between the chlorine partial atomic charge and: (1) the charge averaged over all of the methoxy-ring carbon atoms (Figure 13B); and (2) the total charge of the OxBZ target molecule (Figure 13C and D). These observations are consonant with a classical resonance charge transfer mechanism in which the approaching chlorine atom withdraws electron density primarily from the aromatic methoxy ring during collision leading to Cl-C8 covalent bond formation. The sudden increase in the total electronic charge of the OxBZ target molecule is tantamount to nascent carbocation intermediate formation as chlorine is added to the methoxy ring.

As indicated above, the HO-Cl homolytic bond cleavage resulted in formation of •Cl and •OH radicals. However, as shown in Figure 14, the former was exceedingly ephemeral in nature existing only in a "semi-bound" state around its neutral charge point at about 0.04ps. It then underwent immediate hybridization with the methoxy-ring HOMO orbital at C8 to form the *meta*-stable *ortho*-addition carbocation intermediate.

Key aspects of this proposed mechanism are summarized in Figure 15. Semiempirical RM1/UHF calculations revealed that the major proportion of charge resonance transfer ($\Delta 376e$) occurred at the C8 *ortho*-carbon atom leaving it with a positive partial charge (+0.104e) compared to its original negative charge of -0.272e in the unreacted OxBZ parent. A smaller but still significant charge transfer also took place at the C8 terminal hydrogen whose partial charge transitioned from +0.139e to +0.165e, a decrease of about 0.026e (Figure 15). Though not large in magnitude, it is speculated that electron density was transferred from the terminal hydrogen to chlorine by a delocalization mechanism, possibly involving a direct *"through-space"* inductive (dipole) effect between the hydrogen and chlorine atom [51], or by a relatively weak positive σ-π hyperconjugation mechanism involving a -C-H- sigma-bond alignment with the C8 π bond [39]. Regardless of the delocalization mechanism involved, both C8 and its terminal hydrogen acquired enriched positive charge that would be expected to further destabilize the –C-H-bond, eventually resulting in hydrogen abstraction facilitated by Coulomb repulsion.
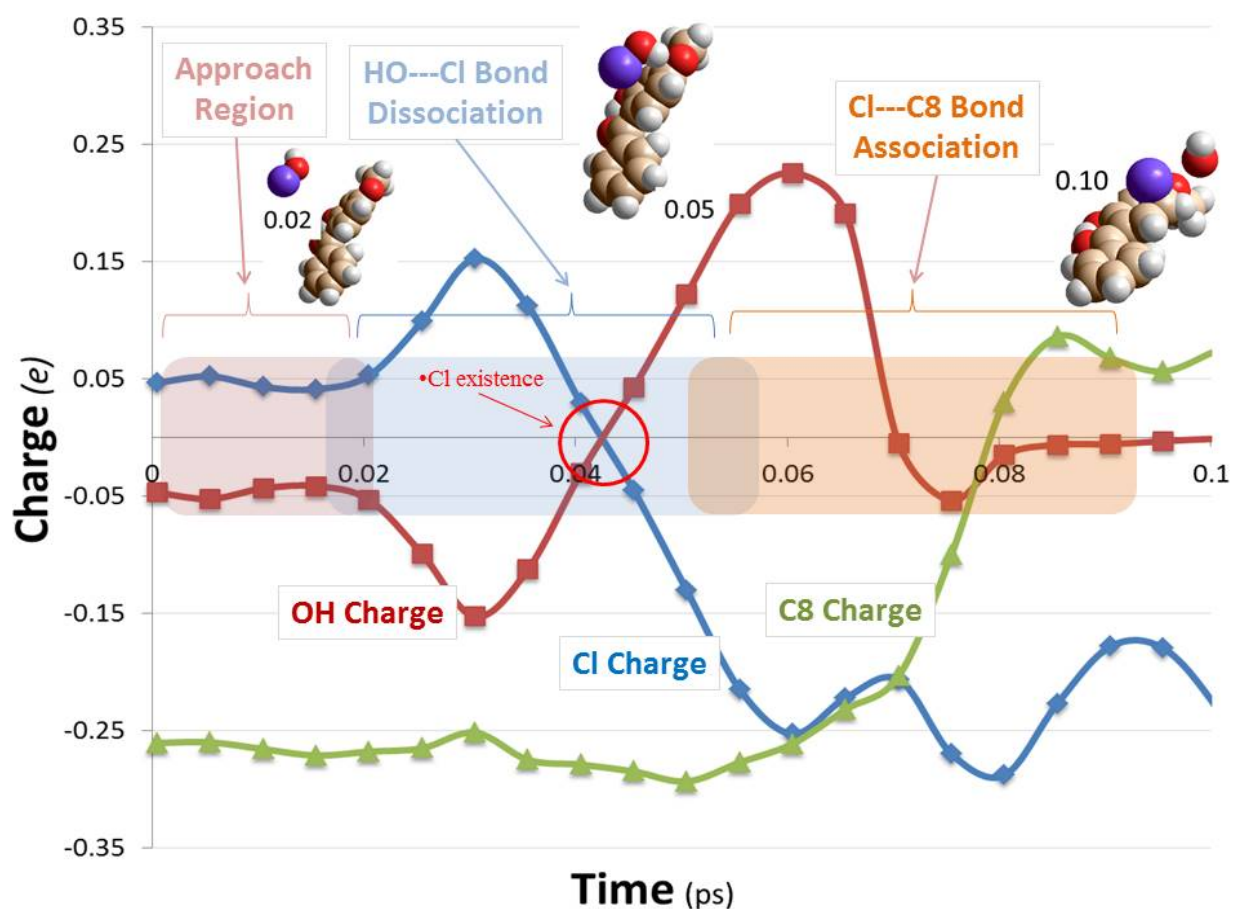
Figure 14. Charge transfer coupling during HO-Cl bond dissociation and Cl-C8 bond formation. Dissociation of the HO-Cl bond was accompanied by transitory existence of a "bound" •Cl radical (red circle) at its charge null point. The Cl and C8 atoms eventually assume equilibrium partial charges (negative for Cl; positive for C8) consistent with Cl-C8 bond covalency. Formation of the •Cl radical was accompanied by release of a free •OH radical. The •Cl radical rapidly undergoes hybridization with atom C8 and the region of the OxBZ (HOMO) orbital associated with the methoxy ring (see Figure 15, below). Note that the charge on the •OH species fluctuates briefly (hysteresis) and mirrors that of the Cl atom, then transitions to $0e$ by about 0.08ps. Inset images show the reaction progress at specified times in ps. Oxygen = red; Chlorine = violet; Carbon = brown; Hydrogen = gray.
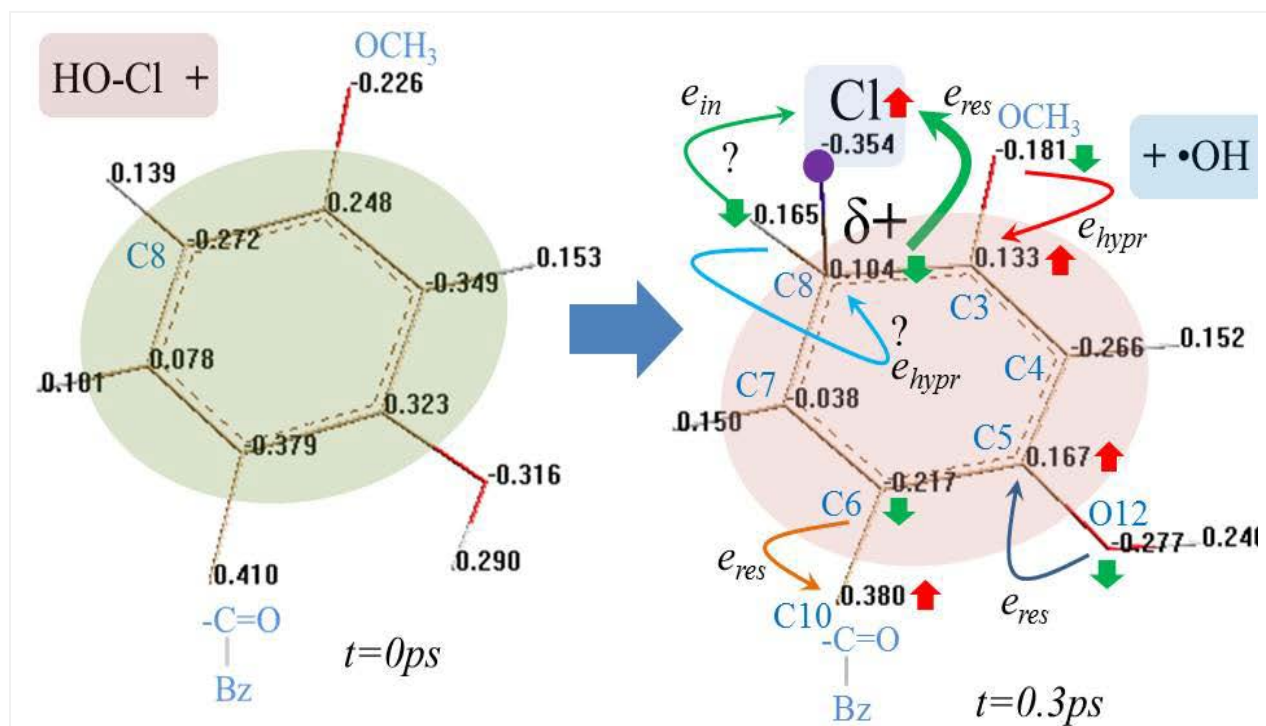
Figure 15. Details of the proposed mechanisms of electrophilic attack at carbon C8 in the methoxy ring of OxBZ to form the *meta*-stable carbocation *ortho*-intermediate shown on the right. Atomic partial charges calculated by RM1/UHF infer charge resonance delocalization (e_{res}) from C8 (thick green arrow) and minor transfer from the C8 terminal hydrogen (thin green and blue arrows), which also becomes more positive. It is unclear (?) if minor charge transfer from the terminal hydrogen could occur by direct inductive polarization (e_{in}) with chlorine (thin green arrow) or by a –C-H- *sigma*-bond hyperconjugation (e_{hypr}) mechanism (blue arrow). Evidence for hyperconjugation at the –OCH$_3$ moiety is indicated by reduction of oxygen partial charge and gain by the *ipso* ring carbon (C3). Note that resonance donation of electron density from the hydroxy oxygen (O12) to the ring (C5), as well as from the ring (C6) to the carbonyl bond (C10) is also consonant with changes in neighbor-atom partial charges. Thick arrows indicate gain (red) or loss (green) of electron density at that locus.

Inspection of the HOMO orbital maps presented in Figure 16 indicates the dissociated chlorine atom underwent rapid hybridization with the OxBZ alpha HOMO orbital with concomitant release of the •OH radical. Moreover, the HOMO orbital energy of OxBZ over the simulation trajectory was directly correlated with a corresponding depression in the chlorine partial charge, an observation that is consistent with a thermodynamically favorable MO rearrangement associated with formation of a nascent *meta*-stable bond between chlorine and C8 in the methoxy ring (see Figure 16, graph inset).
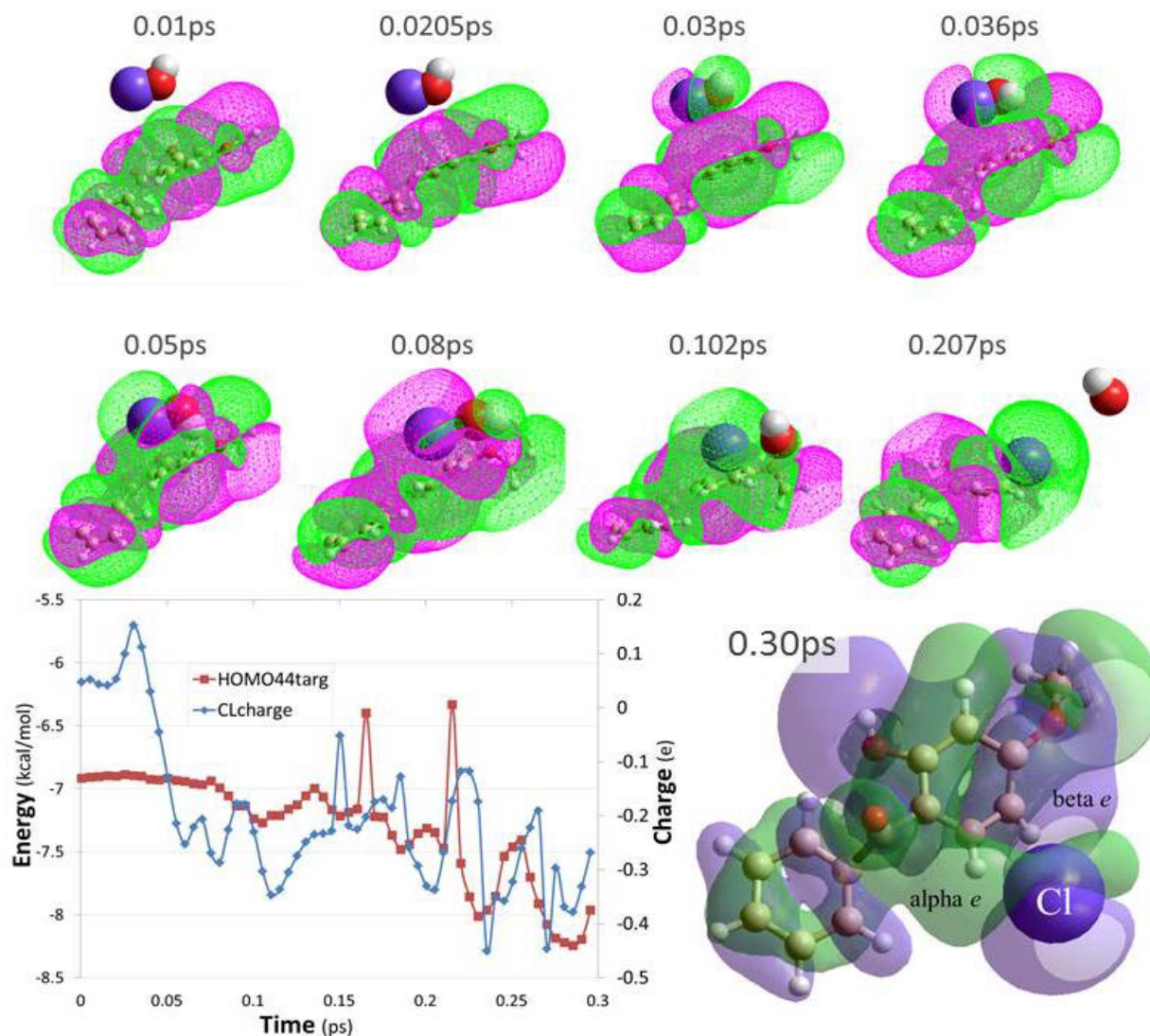

Figure 16. Reaction trajectory frame captures showing progression of HOMO *alpha*- (green) and *beta*-orbital (violet) hybridization of OxBZ with chlorine. Graph inset: Co-plot of partial charge on chlorine atom (CLcharge) versus OxBZ HOMO energy (HOMO44targ) as a function of elapsed time. Orbital energies were calculated by RM1/UHF on the non-optimized structures at each time point. Red = oxygen; Gray = hydrogen; Brown = carbon; Violet = chlorine.

Interatomic π-resonance charge transfer (*i.e.*, electron density delocalization) effects were also recorded between neighboring sp2 carbon atoms comprising the methoxy aromatic ring over the course of the N_{eq}FMD collision trajectory (see Figures 16-17). Neighboring ring-carbon atoms were observed to undergo opposing (*i.e.*, inversely correlated) fluctuations in their RM1/UHF-computed partial electronic charges over the reaction coordinate. For example, an approximate linear direct correlation was observed between the C8 partial atomic charge and the C3-C8 conjugated-bond (stretch) distance (see Figure 17), with shorter C3-C8 bond distances being associated with deeper (more negative) C8 partial charge. This relationship suggests that interatomic conjugated π-bond electron density delocalization was tightly coupled to conformational oscillations in the ring -C-C- bond lengths (and their accompanying MO distortions) arising from kinetic transfer into the OzBZ molecule by prior collision with HOCl. As indicated in Figure 18, such coupled π-bond resonance oscillations were observed for all neighboring pairs of sp2 aromatic carbon atoms comprising the methoxy ring. Partial charges associated with alternating atom pairs, *e.g.*, 3 and 5 or 4 and 6, were directly correlated, whereas charges associated with closest neighbor pairs were inversely correlated as a function of N_{eq}FMD elapsed time.
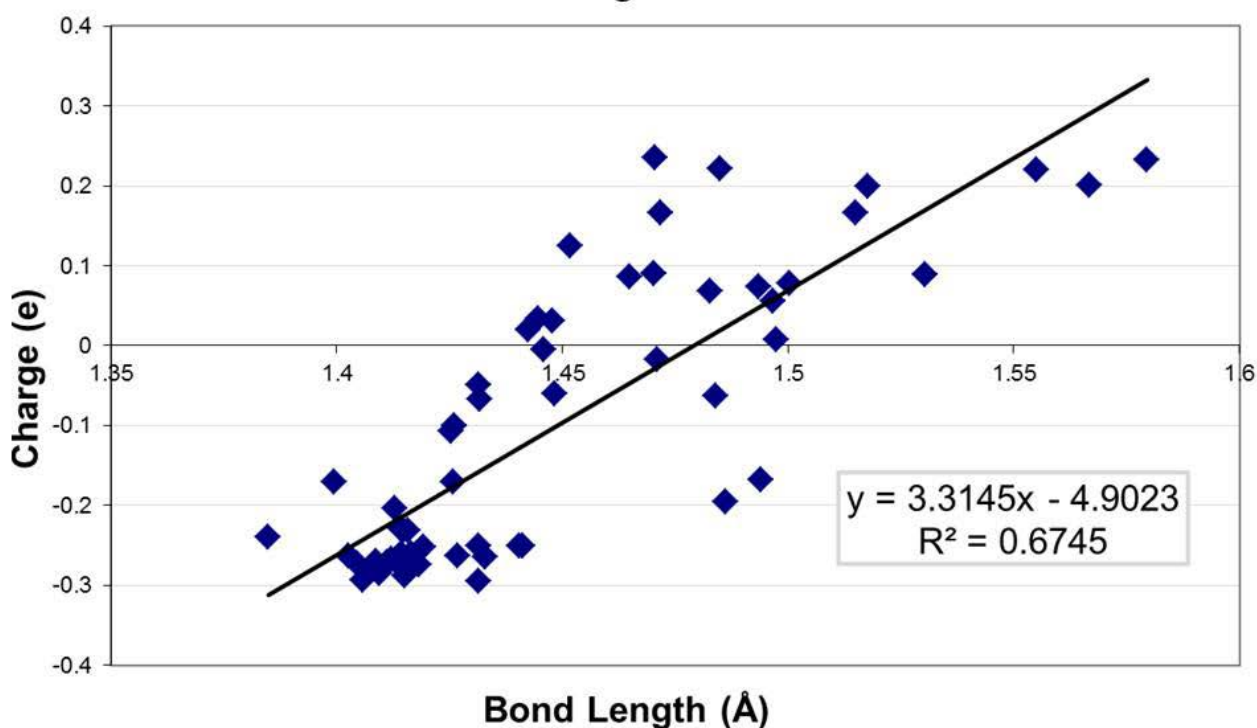

Figure 17. Coupled interatomic π-resonance charge transfer effects in the methoxy ring during chlorine addition to *ortho*-carbon atom C8. In this instance, a positive direct correlation was recorded between the partial atomic charge associated with the sp2 *ortho*-atom C8 as a function of the C3---C8 bond (stretch) length computed over the 0.3ps N_{eq}FMD trajectory.
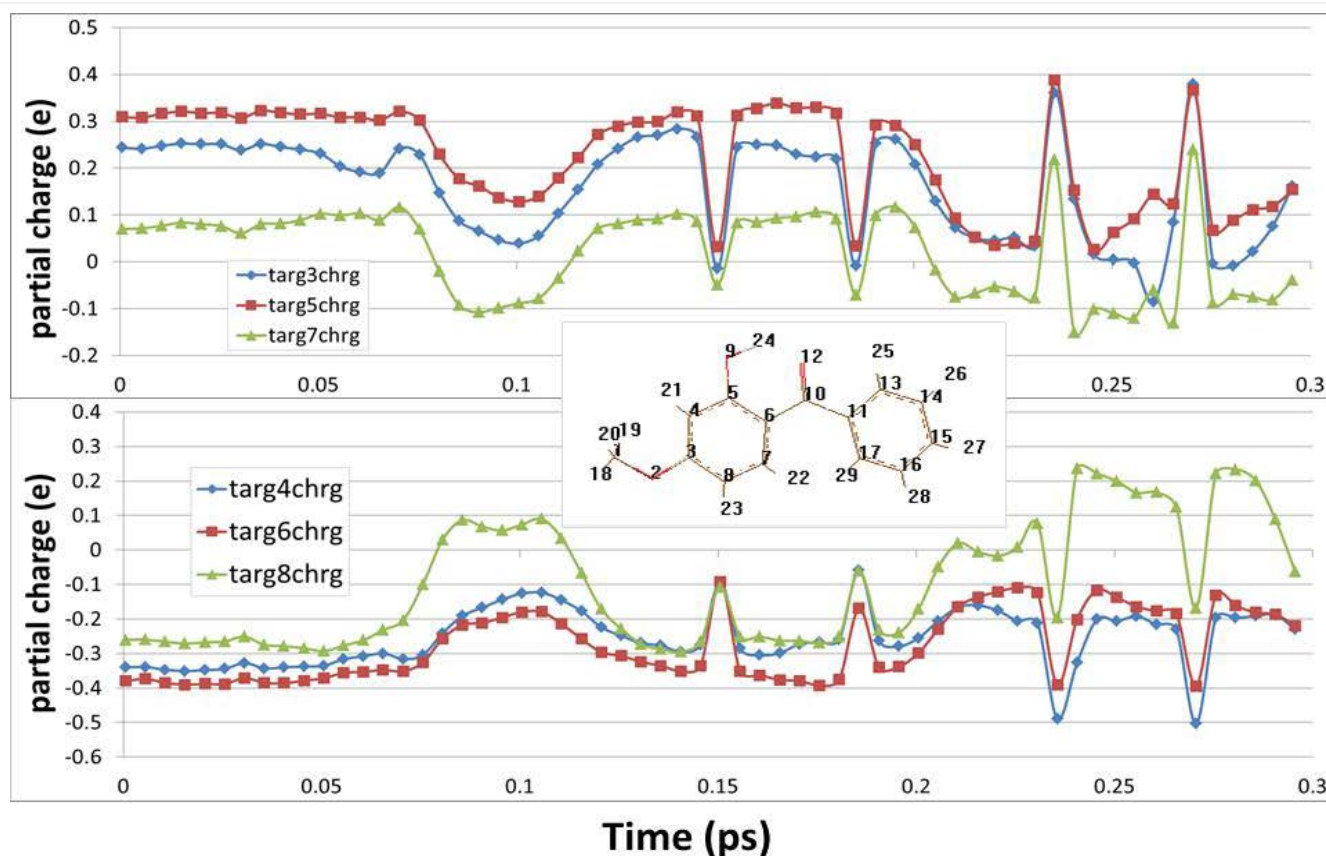
Figure 18. Coupled π-resonance charge transfer fluctuations for all methoxy-ring carbon atoms as a function of N_{eq}FMD elapsed time during chlorine addition to atom C8. Note that partial charge oscillations in alternating methoxy-ring carbon atoms were directly correlated with one another, while charges on closest neighbors were inversely correlated. The atomic charge fluctuations reflected kinetically imposed conformational oscillations resulting from the initial reactive collision between HOCl and OxBZ. Inset gives the OxBZ atom numbering scheme used in this study.

4.7 Formaldehyde Formation by a Di-Radical Mechanism Involving *ipso* Hydroxylation: As indicated above (see Figure 8), a formaldehyde "precursor" was formed in about 0.3% of the N_{eq}FMD simulations. This product was of special interest, not only because it is a known human carcinogen, but also because its formation evidently involved cleavage of the methoxy group; and its mechanism of formation has not been previously described. Based on playback and analysis of Rxn115, which typified this pathway, the main steps involved in formaldehyde formation are proposed in Figure 19A-D. These steps may be summarized as follows:

1. Dissociation of HOCl during its final approach to OxBZ in the vicinity of the methoxy group yielding transitory •OH + •Cl radicals. Reaction "success" was obligatorily correlated with simultaneous arrival of: (a) the chlorine atom proximal to the methyl hydrogen to be

abstracted, and (b) the •OH radical proximal to the methoxy group *ipso* carbon atom (C8). In this orientation, the HOCl molecule was already largely, if not completely, dissociated and positioned with its major (HO-Cl) bond axis more-or-less parallel to that of the O-CH$_3$ methoxy bond (see inset, Figure 19B).

2. Halogen-induced abstraction of one hydrogen atom from the terminal methyl group that rapidly combined with •Cl to form one molecule of HCl.

3. Concomitant with the –CH$_3$ hydrogen abstraction, the •OH radical hydroxylated the C8 *ipso* carbon atom (relative to the methoxy group) causing homolytic cleavage of the C$_{aro}$–O bond and release of an unstable •CH$_2$O• *di*-radical species.

4. The *di*-radical undergoes resonance rearrangement as shown in Figure 19C yielding the resonance-stabilized formaldehyde TP.

It is noteworthy that the reactive collisions resulting in formaldehyde formation were exceedingly sensitive to the reactant starting geometries and orientations, as well as the initial optimized positions of reactive TIP3P water molecules, which in many collisions tended to briefly chaperon (or otherwise interfere with) the HOCl oxidant along its trajectory. As indicated in Figure 19D, very small deviations (<1.5 degrees) in the initial (t=0ps) XYZ axial rotations of the OxBZ (or HOCl) molecule resulted in unproductive reactions, *i.e.*, collisions yielding no formaldehyde formation. On the other hand, by constraining the initial HOCl and OxBZ rotational orientations to predetermined ideal values known to result in formaldehyde formation, it was possible to increase the success rate of formaldehyde formation from about 0.3% to nearly 100% (data not presented).

Finally, the velocity of collision between HOCl and OxBZ were also critical in determining the reaction outcomes and whether formaldehyde would be formed (see Figure 19E). Formaldehyde was only formed within a relatively narrow range of collision velocities (about 90-100 Å/ps). At low collision velocities (*e.g.,* less than about 50Å/ps) the trajectory of HOCl could be slightly altered due to non-bond interactions with proximal water molecules, which tended to exert a relatively greater influence on HOCl transit and orientation leading to unproductive collisions. Lower velocities also were generally unable to overcome non-bond repulsive forces between HOCl and OxBZ, which was a requirement for successful MO hybridizations to occur.
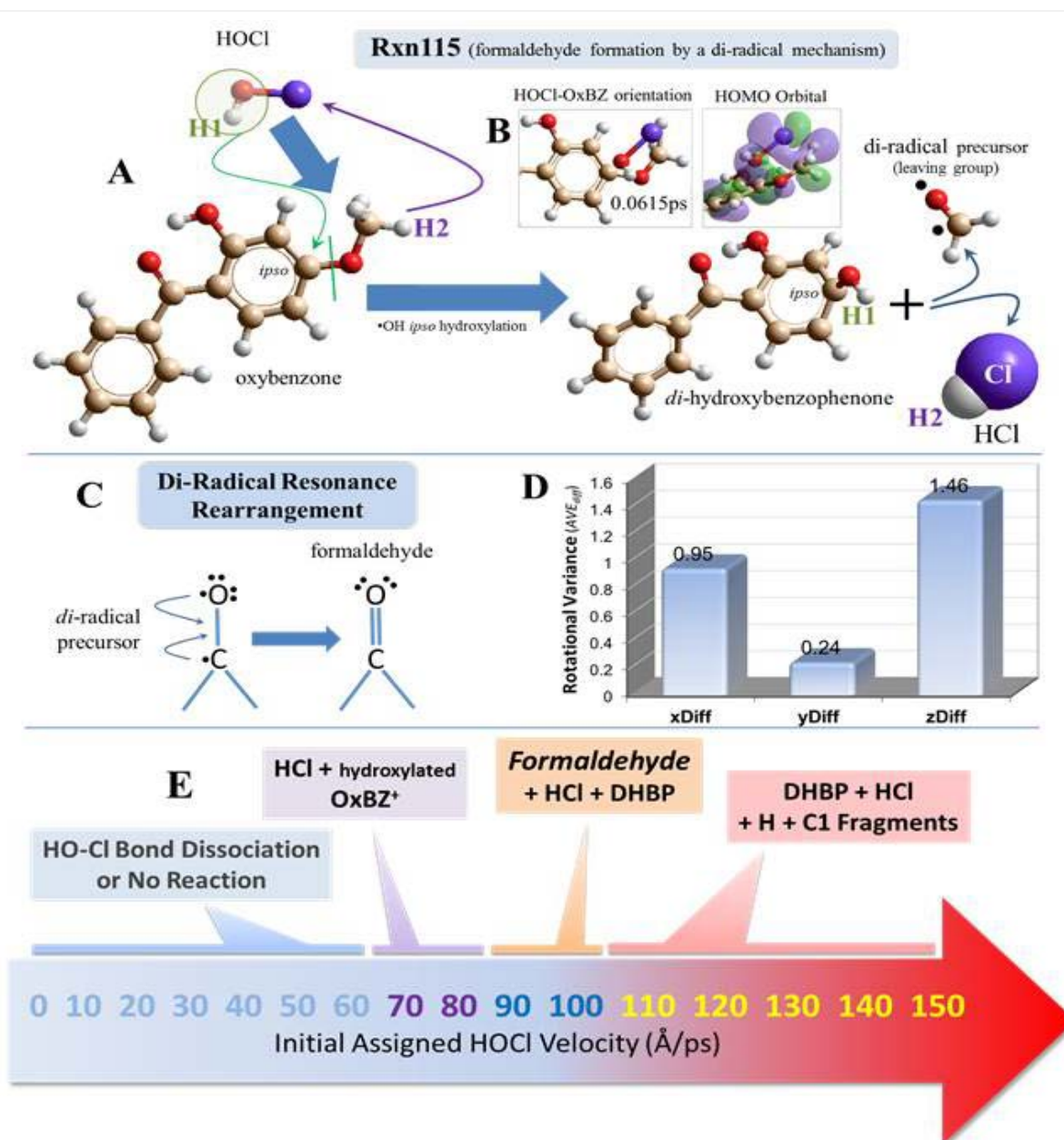
Figure 19. (**A**) Formation of formaldehyde in N_{eq}FMD simulations by *ipso* hydroxylation with release of a •CH$_2$O• *di*-radical leaving group. (**B**) HOCl-OxBZ intermediate orientation at 0.0615ps showing approximate parallel positioning of the HO-Cl bond with that of the O-CH$_3$ bond; and corresponding HOMO orbital hybridization (RM1/UHF). (**C**) Proposed electron delocalization rearrangement yielding the resonance-stabilized formaldehyde TP. (**D**) Differences in degrees in initial average OxBZ axial (XYZ) rotation values at t=0ps for "successful" (yielding formaldehyde) and "unsuccessful" (no formaldehyde formation) collisions. (**E**) Effect of HOCl-OxBZ collision velocity on formaldehyde formation. See text for additional details. Atom colors: Carbon = brown; Oxygen = red; Hydrogen = gray/white; Chlorine = violet.

5.0 Concluding Remarks:

Results presented in this paper demonstrate that N_{eq}FMD reaction simulations can be applied to the detailed analysis of disinfection byproduct (DBP) formation reactions using the sunscreen filter OxBZ as an example. The N_{eq}FMD simulation algorithm is distinguished from other similar approaches by the inclusion of a Newtonian background of explicit water (TIP3P models in this case) approximating the density of normal liquid water. Additionally, water molecules within a user-specified cutoff distance from the reacting species may be included in the reaction coordinate, a feature that allows water to undergo MO rearrangements and interactions with the other reacting species.

Another unique feature of the N_{eq}FMD algorithm is that reaction trajectories can be partitioned into a series of discrete steps or cycles (so-called "quantum runs" or QRs) that allow judicious management of the collision dynamics. For example, as the reactant molecules undergo a forced collision, key parameters, *e.g.*, the MD time step, QR duration (*i.e.*, the QR cycle time), velocity vector, number of QR cycles and so forth, can be independently and automatically adjusted as deemed appropriate after each QR cycle to minimize excessive (repulsive) strain energies, thereby increasing the likelihood of reaction success and minimizing the possibility of calculation failure (by the MD time integrator) due to large energy gradients. Another distinctive aspect of the N_{eq}FMD algorithm is the ability to randomly or systematically modify reactant conformations and orientations at the beginning of each new reaction in a series. Finally, the algorithm is designed to permit the water field to semi-continuously adapt (via MM energy minimizations) to the updated nuclear positions of the reactants following each QR cycle, and *vice versa*.

One potential concern regarding the N_{eq}FMD algorithm is the use of valence-shell semiempirical QM methods (RM1 in this study) for computing MO reorganizations to describe bond dissociation and formation. However, the use of semiempirical methods is rationalized in this study on the basis of: (1) much greater computational efficiency compared to *ab initio* and DFT approaches; (2) reasonable accuracy for most organic compounds in terms of computed geometries, heats of formation, dipole moments, *etc.*, when compared to *ab initio* and DFT calculations [35, 36, 38, 52, 53]; and (3) a history of successful applications of semiempirical QM/MM hybrid methods for modeling enzyme catalysis [24] and many other chemical processes [22]. Significantly, the use of core-core interaction terms and other empirical parameters and formal approximations in RM1 and related "neglect of diatomic differential overlap" (NDDO) methods partially compensates for the lack of explicit treatment of electron correlation [35].

In the current investigation, RM1/UHF calculations as implemented in the N_{eq}FMD algorithm qualitatively emulated certain key aspects of substituent directing and activating effects. In particular, the N_{eq}FMD algorithm forecast the activating influence of the electron donating -OH and -OCH$_3$ side groups on the OxBZ methoxy aromatic ring, as well as the deactivating influence

of the central carbonyl linkage on the unsubstituted benzene ring. Furthermore, the expected *ortho*-directing effect of the -OH and -OCH$_3$ groups were clearly observed in phenol and anisole, respectively. Although *para*-direction was weak for these test compounds, it was nevertheless evident to a minor degree (see Figure 7, above). The expected *para*-directing influence of the methoxy group at atom 6, as well as the expected *ortho*-directing effect of the –OH group at this same position, were likely suppressed to a significant degree by the deactivating and *meta*-directing behavior of the adjacent carbonyl bond. For the test compound aniline, the primary amine (-NH$_2$) exerted pronounced *ortho/para* direction, as would be anticipated for this donating group.

Although not quantitatively evaluated in this study, elevated halogen addition at the methoxy group *ipso* position of OxBZ (atom C3) may have been caused by: (1) underestimation of –O-C-H hyperconjugation effects by RM1 at this position, which would effectively delocalize more electron density from oxygen lone pairs to the ring; or (2) poor alignment of the –O-C-H π-σ* bond due to conformational fluctuations at or around this substituent group. Hyperconjugation is known to be extremely sensitive to steric effects [39, 40]. Anomalous chlorine addition at the *meta*-position of phenol, was unforeseen and cannot be easily reconciled without additional research, perhaps focused on the systematic evaluation of alternative semiempirical QM methods (or parameters) and MM force fields (*e.g.,* OPLS for liquid solutions).

In this study, only 1st-generation TPs were analyzed, *i.e.*, initial TPs originating from bi-molecular HOCl collisions *with only the parent target compound*. However by cycling the N_{eq}FMD algorithm over 1st-generation TPs of interest, it is possible to explore the formation of 2nd- and later-generation TPs, as recently described by Ridgway *et al.* [30] for reactions of certain volatile gas-phase organics with ozone.

Because collision durations were purposely restricted to <0.5ps to maximize the number of reactions in a series, the N_{eq}FMD algorithm as applied in this investigation did not allow sufficient time for potentially energetically favorable molecular (MO) rearrangements to take place, particularly for *meta*-stable (carbocation) intermediates, such as a *meta* → *ortho* migration of a halogen atom, or a hydrogen abstraction from a halogenated Wheland intermediate. It should be emphasized, however, that such rearrangements can indeed be explored for specific TPs of interest by subsequently carrying out conventional equilibrium MD using temperatures high enough to sample rearrangement barriers.

As applied to OxBZ, the N_{eq}FMD algorithm revealed a range of TPs, including a number that have been previously experimentally verified by other researchers [16, 20]. Transformation products observed in the N_{eq}FMD simulations as well as in experimental studies included *mono*-chlorinated OxBZ (especially the *ortho*-addition product), *mono*-chlorobenzene, •OH radicals, HCl, chloromethane, hydrogen abstracted TPs, and open-ring and carbonyl-bond scission products [16-20].

Several other compounds that have not yet been experimentally verified were also observed, including mono-chloroguaiacol (*ortho*-chloromethoxyphenol), *mono*-chlorohydroxybenzophenone, *di*-hydroxybenzophenone, 4-methoxycatechol, hydroxymethoxybenzaldehyde (precursor), benzaldehyde (precursor) and formaldehyde (*di*-radical precursor). At least some of these compounds (*e.g.,* mono-chloroguaiacol and 4-methoxycatechol) have been demonstrated to exhibit human and/or environmental health hazards, including cytotoxicity, mutagenicity, and carcinogenic activity [54, 55].

In addition to yielding a statistical distribution of expected TPs, as well as some compounds and intermediates that have not been previously reported, the N_{eq}FMD algorithm was used to analyze the formation of a *ortho*-halogenated Wheland adduct of OxBZ. This *meta*-stable intermediate compound was of special interest since the stable hydrogen abstracted end-product was reported by Zhang *et al.* [16] and others [20]. Analysis of N_{eq}FMD collision trajectories for this reaction revealed a *pseudo*-stable Cl-adduct formation that occurred by electrophilic attack at methoxy ring atom C8 situated *ortho* to the –OCH₃ group and *para* to the –OH group. A critical step in the reaction path was homolytic cleavage of the relatively labile HO-Cl bond in hypochlorous acid followed by release of a free •OH radical and a transitory "semi-bound" •Cl radical. The later initiated electron delocalization by a π-resonance charge transfer mechanism in which electron density transmigrated from the methoxy ring to chlorine, resulting in rapid covalent bond formation (<50 fs). It was also noted that conjugated π-bond resonance fluctuations in the OxBZ methoxy ring were tightly coupled to kinetically-invoked conformational oscillations stemming from the initial collision event with HOCl.

Collision orientation during N_{eq}FMD simulations was critical to determining whether a reaction proceeded to completion (*i.e.*, whether specific TP formation occurred). Very subtle alterations in the starting conformations and orientations of the reactants completely changed the reaction dynamics and the kinds of TPs generated (data not shown). Solvent effects in the form of Coulomb and Lennard-Jones interactions with the reactants, as well as random steric interference along the reaction trajectories, also influenced the N_{eq}FMD collision orientations and reaction outcomes. These observations argue for the importance of reaction "preorganizational steps" as described by Rosokha and Kochi [56] in which ephemeral semi-stable pre-equilibrium (arene) complexes evolve through inductive and/or resonant charge transfer processes between non-bonded species prior to formation or dissociation of covalent bonds. Formation of the *meta*-stable halogen-addition OxBZ intermediate described in this report or the formaldehyde *di*-radical intermediate, are two examples of preorganizational states that would be expected to undergo MO rearrangements leading to stable TPs.

Recently Galabov *et al.* [49] challenged the traditional view of electrophilic aromatic addition/substitution reactions involving the standard S$_E$Ar (arenium ion) mechanism. Using computational and NMR approaches, they identified two alternative reaction pathways, an "addition–elimination" sequence and a "direct concerted mechanism", with the former being more favorable with slightly lower activation barriers. According to the authors, no arenium σ-

complex is found along the reaction path for direct substitution, yet several new hybrid carbocation-HCl intermediates are proposed that respond to autocatalytic HCl elimination yielding the *ortho* product. Either alternative explained the preference for *ortho/para* anisole derivatives, since these orientations represent a natural consequence of the favored stabilizing influence of the -OCH$_3$ group.

Although HCl formation was observed in a significant fraction of the HOCl-OxBZ and other reactions performed in this study (data not shown), no compelling evidence was observed for the formation of HCl-carbocation complexes. However, notwithstanding a more conventional interpretation, it would be possible to interpret the nascent H---C$_{aro}$---Cl bond as the earliest stage of such a putative complex. Indeed, as suggested by data presented in Figures 15-18, coupled changes in the atomic partial charges of the participating atoms (*i.e.*, the terminal H---C$_{aro}$- and Cl---C$_{aro}$-) could have interacted through an inductive mechanism not unlike that described by Galabov *et al.* [49].

Based on the findings reported in this investigation, it is concluded that N_{eq}FMD simulations can be successfully applied in combination with experimental approaches to help elucidate the roles of transitory or semi-stable intermediates that are sometimes challenging to detect and quantify in complex chemical reaction pathways. The modeling approach could be expected to have broad application in identifying potential reaction intermediates that cannot be readily experimentally observed, as well as in deciphering other details of proposed TP formation pathways.

6.0 References:

1. M.S. Latha, J. Martis, V. Shobhav, R.S. Shinde, S. Bangera, B. Krishnankutty, S. Bellary, S. Varughese, P. Rao, and B.R.N Kumar, Sunscreening agents: a review, J. Clin. Aesthet. Dermatol., 6 (2013) 16-26.

2. A.J.M. Santos, M.S. Miranda and J.C.G.E da Silva, The degradation products of UV filters in aqueous and chlorinated aqueous solutions, Water Res., 46 (2012) 3167-3176.

3. S. Kim and K. Choi, Occurrences, toxicities, and ecological risks of benzophenone-3, a common component of organic sunscreen products: a mini-review, Environ Int., 70 (2014) 143-57.

4. M.E. Balmer, H.R. Buser, M.D. Müller and T. Poiger, Occurrence of some organic UV filters in wastewater, in surface waters, and in fish from Swiss lakes, Environ. Sci. Technol., 39 (2005) 953-62.

5. C.A. Downs, E. Kramarsky-Winter, R. Segal, J. Fauth, S. Knutson, O. Bronstein, F.R. Ciner, F.R., J. Rina, Y. Lichtenfeld, C.M. Woodley, P. Pennington, K. Cadenas, A. Kushmaro and Y. Loya, Toxicopathological effects of the sunscreen UV filter, oxybenzone (benzophenone-3), on coral planulae and cultured primary cells and its environmental contamination in Hawaii and the U.S. Virgin Islands, Arch. Environ. Contam. Toxicol., 70 (2015) 265–288.

6. G. Kerdivel, R.L. Guevel, D. Habauzit, F. Brion, S. Ait-Aissa and F. Pakdel, Estrogenic potency of benzophenone UV filters in breast cancer cells: proliferative and transcriptional activity substantiated by docking analysis, PLOS ONE 8 (2013) e60567.

7. M. Coronado, H. De Haro, X. Deng, M.A. Rempel, R. Lavado and D. Schlenk, Estrogenic activity and reproductive effects of the UV-filter Oxybenzone (2-hydroxy-4-methoxyphenyl-methanone) in fish, Aquatic Toxicol., 90 (2008) 182–187.

8. M. Schlumpf, S. Durrer, O. Faass, C. Ehnes, M. Fuetsch, C. Gaille, M. Henseler, L. Hofkamp, K. Maerkel, S. Reolon, B. Timms, J.A.F. Tresguerres and W. Lichtensteiger, Developmental toxicity of UV filters and environmental exposure: a review, Internatl. J. Androl., 31 (2008) 144–151.

9. K.M. Hanson, E. Gratton and C.J. Bardeen, Sunscreen enhancement of UV-induced reactive oxygen species in the skin, Free Radical Biol. Med., 41 (2006) 1205–1212.

10. D. Nakajima, S. Asada, S. Kageyama, T. Yamamoto, H. Kuramochi, N. Tanaka, K. Takeda and S. Goto, Activity related to the carcinogenicity of plastic additives in the benzophenone group, J. UOEH, 28 (2006) 143-56.

11. H. Zhao, D. Wei, M. Li and and Y. Du, Substituent contribution to the genotoxicity of benzophenone-type UV filters, Ecotoxicol. Environ. Safety, 95 (2013) 241–246.

12. M.C. Cuquerella, V. Lhiaubet-Vallet, J. Cadet and M.A. Miranda, Benzophenone photosensitized DNA damage, Acc. Chem. Res., 45 (2012) 1558–1570.

13. S.J. In, S.-H. Kim, R.E. Go, K.A. Hwang and K.-C. Choi, Benzophenone-1 and nonylphenol stimulated MCF-7 breast cancer growth by regulating cell cycle and metastasis-related genes via an estrogen receptor α-dependent pathway, J. Toxicol. Environ. Health, A78 (2015) 492-505.

14. S.-H. Kim, K. Hwang, S.-M. Shim and K.-C. Choi, Growth and migration of LNCaP prostate cancer cells are promoted by triclosan and benzophenone-1 via an androgen receptor signaling pathway, Environ. Toxicol. Pharmacol., 39 (2015) 568-576.

15. P.P. Phiboonchaiyanan, K. Busaranon, C. Ninsontia and P. Chanvorachote, Benzophenone-3 increases metastasis potential in lung cancer cells via epithelial to mesenchymal transition, Cell Biol. Toxicol., 33 (2017) 251–261.

16. S. Zhang,. X. Wang, H. Yang and Y.F. Xie, Chlorination of oxybenzone: Kinetics, transformation, disinfection byproducts formation, and genotoxicity changes, Chemosphere, 154 (2016) 521-527.

17. A. Gackowska, M. Przybyłek, W. Studziński and J. Gaca, Formation of chlorinated breakdown products during degradation of sunscreen agent 2-ethylhexyl-4-methoxycinnamate in the presence of sodium hypochlorite, Environ. Sci. Pollut. Res., 23 (2016) 1886–1897.

18. J. Li, L.-Y. Ma and L. Xu, Transformation of benzophenone-type UV filters by chlorine: kinetics, products identification and toxicity assessments, J. Haz. Mat., 311 (2016) 263-272.

19. S.E. Duirk, D.R. Bridenstine and D.C. Leslie, Reaction of benzophenone UV filters in the presence of aqueous chlorine: Kinetics and chloroform formation, Water Res., 47 (2013) 579-587.

20. N. Negreira, P. Canosa, I. Rodrıguez, M. Ramil, E. Rubı and R. Cela, Study of some UV filters stability in chlorinated water and identification of halogenated by-products by gas chromatography–mass spectrometry, J. Chromatog., A (2008) 1178, 206–214.

21. O. Acevedo, Simulating chemical reactions in ionic liquids using QM/MM methodology, J. Phys. Chem. A118 (2014) 11653–11666.

22. G. Groenhof, Introduction to QM/MM simulations, In: L. Monticelli and E. Salonen (eds.), Biomolecular Simulations: Methods and Protocols, Methods in Molecular Biology, Springer Science+Business Media New York, 2013, vol. 924, Chapter 3, pp. 43-65.

23. M.W. van der Kamp and A.J. Mulholland, Combined quantum mechanics/molecular mechanics (QM/MM) methods in computational enzymology, Biochem., 16 (2013) 2708–2728.

24. H.M. Senn and W. Thiel, QM/MM methods for biomolecular systems, Angew. Chem. Int., 48 (2009) 1198–1229.

25. A.S. Gonçalves, T.C.C. França, J.D. Figueroa-Villar and P.G. Pascutti, Molecular dynamics simulations and QM/MM studies of the reactivation by 2-PAM of Tabun-inhibited human acethylcolinesterase, J. Braz. Chem. Soc., 22 (2011) 155-165.

26. K.W. Sattelmeyer, J. Tirado-Rives and W.L. Jorgensen, Comparison of SCC-DFTB and NDDO-based semiempirical molecular orbital methods for organic molecules, J. Phys. Chem., A50 (2006) 13551–13559.

27. M.P. Repasky, J. Chandrasekar and W. Jorgensen, PDDG/PM3 and PDDG/MNDO: improved semiempirical methods, J. Comput. Chem., 23 (2002) 1601–1622.

28. S. Antonczak, M. Ruiz-López and J.-L. Rivail, The hydrolysis mechanism of formamide revisited: comparison between *ab initio*, semiempirical and DFT results, J. Mol. Model., 3 (1997) 434–442.

29. J.J. Dannenberg, Hydrogen bonds: a comparison of semiempirical and *ab initio* treatments, J. Molec. Struc. THEOCHEM, 401 (1996) 279-286.

30. H.F. Ridgway, B. Mohan, X. Cui, K.J. Chua and M.R. Islam, Molecular dynamics simulation of gas-phase ozone reactions with sabinene and benzene, J. Molec. Graphics and Modelling, 74 (2017) 241–250.

31. G.B. Rocha, R.O. Freire, A.M. Simas and J.P. Stewart, RM1: a reparameterization of AM1 for H, C, N, O, P, S, F, Cl, Br, and I, J. Comp. Chem., 27 (2006) 1101-1111.

32. W.L. Jorgensen, J. Chandrasekhar, J.D. Madura, R.W. Impey and M.L. Klein, Comparison of simple potential functions for simulating liquid water, J. Chem. Phys., 79 (1983) 926.

33. P. Pulay, Convergence acceleration of iterative sequences: the case of SCF iteration, Chem. Phys. Lett., 73 (1980) 393–398.

34. P. Pulay, Improved SCF convergence acceleration, J. Comp. Chem., 3 (1982) 556–560.

35. A.S. Christensen, T. Kubar, Q. Cui and M. Elstner, Semiempirical quantum mechanical methods for noncovalent interactions for chemical and biochemical applications, Chem. Rev., 116 (2016) 5301–5337.

36. M.S. Elioff, J. Hoy and J.A. Bumpus, Calculating heat of formation values of energetic compounds: a comparative study, Adv. Phys. Chem., Article ID 5082084(2016) 1-10.

37. R. Casadesús, M. Moreno, A. González-Lafont, J.M. Lluch and M.P. Repasky, Testing electronic structure methods for describing intermolecular H...H interactions in supramolecular chemistry, J. Comp. Chem., 25 (2004) 99-105.

38. I. Tubert-Brohman, C.R. Guimarães, M.P. Repasky and W.L. Jorgensen, Extension of the PDDG/PM3 and PDDG/MNDO semiempirical molecular orbital methods to the halogens, J. Comp. Chem., 25 (2004) 138-50.

39. I.V. Alabugin and T.A. Zeidan, Stereoelectronic effects and general trends in hyperconjugative acceptor ability of σ-bonds, J. Am. Chem. Soc., 124 (2002) 3175-3185.

40. I.V. Alabugin, K.M. Gilmore and P.W. Peterson, Hyperconjugation, Comp. Molec. Sci., 1 (2011) 109-141.

41. K. Bozorov, J.-U. Zhao and H.A. Aisa, Recent advances in *ipso*-nitration reactions. Archive Organ. Chem., Arkivoc part I (2017) 41-66.

42. T. Ohe, T. Mashino and M. Hirobe, Substituent elimination from *p*-substituted phenols by cytochrome P450: *ipso*-substitution by the oxygen atom of the active species, Drug Metabol. Disposition, 25 (1996) 116-122.

43. B. Kolvenbach, N. Schlaich, Z. Raoui, J. Prell, S. Zuhlke, A. Schaffer, F.P. Guengerich and P.F.X. Corvini, Degradation pathway of bisphenol A: does *ipso* substitution apply to phenols containing a quaternary *alpha*-carbon structure in the *para* position?, Appl. Environ. Microbiol., 73 (2007) 4776–4784.

44. F.L. Gabriel, M. Cyris and G.W. Kohler, *Ipso*-substitution: a general biochemical and biodegradation mechanism to cleave alpha-quaternary alkylphenols and bisphenol A, Chem. Biodivers., 9 (2007) 2123-37.

45. A. Fischer and G. Henderson, Bromination of phenols, isomerization and disproportionation of bromophenols, and dienone-phenol rearrangement of bromodienones, Can. J. Chem., 61 (1983) 1045-1053.

46. Y. Ogata, M. Kimura, Y. Kondo, H. Katoh and F.-C. Chen, Orientation in the chlorination of phenol and of anisole with sodium and t-butyl hypochlorites in various solvents, J. Chem. Soc., Perkin Trans., 2 (1984) 451-453.

47. J.J. Mullins, Hyperconjugation: A more coherent approach, J. Chem. Educ., 89 (2012) 834-836.

48. R.K. Bansal, N. Gupta and S. Bansal, Semiempirical PM3 calculations of pyridinium dichlorophosphinomethylides: presence of negative hyperconjugation, Indian J. Chem., 43B (2004) 144-148.

49. B. Galabova, G. Kolevaa, S. Simova, B. Hadjieva, H.F. Schaefer and P.V.R Schleyer, Arenium ions are not obligatory intermediates in electrophilic aromatic substitution, Proc. Natl. Acad. Sci., 111 (2014) 10067-10072.

50. T. Manasfi, V. Storck, S. Ravier, C. Demelas, B. Coulomb and J.-L. Boudenne, Degradation products of benzophenone-3 in chlorinated seawater swimming pools, Environ. Sci. Technol., 49 (2015) 9308–9316.

51. J.F. Bunnet, Physical Organic Terminaology, after Ingold, Bull. Hist. Chem., 19 (1996) 33–42.

52. J.J.P. Stewart, Optimization of parameters for semiempirical methods V: modification of NDDO approximations and application to 70 elements, J. Mol. Model, 13 (2007) 1173-1213.

53. J. Dolenc and J. Koller, An improved semiempirical MO PM3 method for hydrogen-bonded systems, Acta Chim. Slov., 53 (2006) 229-237.

54. E.O. Igbinosa, E.E. Odjadjare, V.N. Chigor, I.H. Igbinosa, A.O. Emoghene, F.O. Ekhaise, N.O. Igiehon and O.G. Idemudia, Toxicological profile of chlorophenols and their derivatives in the environment: the public health perspective, Sci. World J., Article ID 460215 (2013) 1-11.

55. J. Michałowicz and I. Majsterek, Chlorophenols, chlorocatechols and chloroguaiacols induce DNA base oxidation in human lymphocytes (in vitro), Toxicol., 268 (2010) 171–175.

56. S. Rosokha and J.K. Kochi, The preorganization step in organic reaction mechanisms: charge transfer complexes as precursors to electrophilic aromatic substitutions, J. Org. Chem., 67 (2002) 1727–1737.